

THESIS

PATTERNS IN DYNAMICS

Submitted by

Francis C. Motta

Department of Mathematics

In partial fulfillment of the requirements

For the degree of Master of Science

Colorado State University

Fort Collins, Colorado

Spring 2012

Master's Committee:

Advisor: Patrick D. Shipman

R. Mark Bradley  
Renzo Cavalieri  
Gerhard Dangelmayr

Copyright by Francis Charles Motta 2012

All Rights Reserved

## ABSTRACT

### PATTERNS IN DYNAMICS

In this paper we introduce and explore the idea of persistent homology (PH) and discuss several applications of this computational topology tool beyond its intended purpose. In particular we apply persistence to data generated by dynamical systems. The application of persistent homology to the circle map will lead us to rediscover the well-known result about the distribution of points in the orbit of this ergodic system called the Three Distance Theorem. We then apply PH to data extracted from several models of ion bombardment of a solid surface. This will present us with an opportunity to discuss new ways of interpreting PH data by introducing statistics on its output. Using these statistics we will begin to develop a technique to answer questions of interest to physicists about the degree of ordering present in the topography of a solid surface after ion bombardment. Finally we observe some inherent limitations in PH and, through simple examples, develop techniques to improve the technology. Specifically we will implement algorithms to iteratively spread points on a real algebraic variety and demonstrate that the methodology works to improve the signals in the output of PH.

## ACKNOWLEDGEMENTS

The author would like to thank his entire committee for taking the time to read this thesis. He would also like to specifically thank his advisor Dr. Patrick Shipman for his infinite patience and perpetual support of exploring new ideas, Dr. R. Mark Bradley for valuable and grounding discussions, and Dr. Chris Peterson for his insights into persistent homology and his ideas on how to apply it and improve it.

## TABLE OF CONTENTS

<b>1 INTRODUCTION</b>	<b>1</b>
<b>2 PERSISTENT HOMOLOGY</b>	<b>2</b>
2.1 Simplicial Homology . . . . .	2
2.2 The Rips Complex . . . . .	8
2.3 Barcodes . . . . .	11
<b>3 THE CIRCLE MAP</b>	<b>13</b>
3.1 Continued Fractions . . . . .	16
<b>4 ION BOMBARDMENT</b>	<b>25</b>
4.1 Linear Stability Analysis . . . . .	27
4.2 Non-Linear Analysis . . . . .	31
4.3 Persistent Homology Statistics . . . . .	37
<b>5 IMPROVING PH SAMPLES</b>	<b>43</b>
<b>6 OUTLOOK</b>	<b>51</b>

## LIST OF FIGURES

2.1 Geometric simplicial complexes. . . . .	3
2.2 2-dimensional simplicial complex. . . . .	7
2.3 Sequence of simplicial complexes using Rips method. . . . .	10
2.4 Barcodes displaying the transition times where Betti numbers change. . . . .	11
3.1 100/800 iterations of the circle/modified circle map with angle a) $\left\{ \frac{1+\sqrt{5}}{2} \right\}$ and b) π. . . . .	14
3.2 Rips barcodes of 100 iterations of the modified circle map with angle a) $\left\{ \frac{1+\sqrt{5}}{2} \right\}$ and b) π. . . . .	15
3.3 Betti-0 barcodes for orbits under $T_\phi$ of various length . . . . .	15
3.4 Betti-0 barcode produced from the the first 17 points in the forward orbit of 0 under $T_{\sqrt[3]{2}}$ . . . . .	22
4.1 (i) The $ac$ -plane partitioned into regions based on the types of bifurcations which can occur. For example above the line $a = c$ , either $b_{T,x}$ or $b_{T,y}$ will be the critical value of $b$ (depending on which is larger). On the line $a = c$ we have $b_{T,y} = a =: b_{II,y}$ and below the $a = c$ line $b_{T,y}$ is no longer valid; here either $b_{T,x}$ or $b_{II,y}$ will be the critical value of $b$ (depending on which is larger). Similar reasoning shows a transition along the $c = \frac{a}{r_1}$ line, which can be above or below the $a = c$ line depending on the choice of $r_1$ . (ii) The prototypical regions where $\text{Re}(\sigma_+(\vec{k})) > 0$ associated to the various critical values of $b$ . . . .	30
4.2 Plots of $b_{T,x}$ and $b_{T,y}$ as functions of $r = r_1 = r_2$ showing points and regions of interest. . . . .	30
4.3 A defect in a hexagonal lattice which results in a hole (a topological circle) ap- pearing at filtration time $t =  u_1 $ . . . . .	38
4.4 A time series of plots of $u(x, y, t)$ evolving according to the coupled equations 4.1, 4.2 with parameters $a = .4, c = .6, r_1 = r_2 = r_3 = 1, \lambda = -.3$ in a square re- gion ( $-120 \leq x, y \leq 120$ ) at times (1a-e) $t = 200$ , (2a-e) $t = 1,800$ , (3a-e) $t = 9,800$ , (4a-e) $t = 30,000$ . These show the evolution towards a hexago- nal array. (1-4a) shows the surface plots where lighter regions indicate larger values of $u(x, y, t)$ . (1-4b) shows the same surface plots with the local max- ima [17] (peaks of the nanodots) highlighted by a blue dot. (1-4c) shows plots of these peaks with the surface plot removed. (1-4d) are the Betti-0 barcodes generated by the blue points, considered as a sample of the plane. (1-4e) are the Betti-1 barcodes generated by the blue points, considered as a sample of the plane. . . . .	40

4.5 A time series of plots of $u(x, y, t)$ evolving according to the isotropic KS equation 4.3 with parameters $r_1 = r_3 = 1, \lambda = -.3$ in a square region ( $-120 \leq x, y \leq 120$ ) at times (1a-e) $t = 200$ , (2a-e) $t = 1,800$ , (3a-e) $t = 9,800$ , (4a-e) $t = 30,000$ . (1-4a) shows the surface plots where lighter regions indicate larger values of $u(x, y, t)$ . (1-4b) shows the same surface plots with the local maxima [17] (peaks of the nanodots) highlighted by a blue dot. (1-4c) shows plots of these peaks with the surface plot removed. (1-4d) are the Betti-0 barcodes generated by the blue points, considered as a sample of the plane. (1-4e) are the Betti-1 barcodes generated by the blue points, considered as a sample of the plane. . . . .	41
4.6 Plot of the average Betti-1 barcode lengths as a function of time in timesteps of $\Delta t = 200$ for the range of times $200 \leq t \leq 30,000$ for the simulation presented in Figure 4.4 . . . . .	42
4.7 Plot of the average Betti-1 barcode lengths as a function of time in timesteps of $\Delta t = 200$ for the range of times $200 \leq t \leq 30,000$ for the Kuramoto-Sivashinsky equation with parameters $r_1 = r_3 = 1, \lambda = -.3$ in the domain $-120 \leq x, y \leq 120$ . . . . .	42
5.1 Two different samples of circle and their corresponding Betti-0 and Betti-1 barcodes. (a) is an example of an evenly distributed sample while (b) is a poorly distributed sample. . . . .	43
5.2 Snapshots at iteration numbers (a) 10, (b) 15, and (c) 20, showing the evolution of the position of the sample points as they push against each other according to a $\frac{1}{r^2}$ Coulomb's law. . . . .	45
5.3 (a) Barcodes generated by a random sample of $n = 40$ orthogonal $2 \times 2$ matrices and (b) barcodes after the sample is allowed to evolve under iterations of the algorithm described above. . . . .	47
5.4 Samples of $n = 150$ points on the torus given by Equation 5.1, Betti-0, Betti-1, and Betti-3 barcodes for the associated sample taken at (i) 1, (ii) 30, (iii) 60, (iv) 90, (v) 120, and (vi) 150 iterations of the spreading procedure. . . . .	49

## LIST OF TABLES

2.1	Persistent homology data . . . . .	10
3.1	Betti-0 data for orbit of $x = 0$ of length $n$ under $T_\phi$ . Highlighted transition times indicate first occurrence of these new transition times. . . . .	16
3.2	Betti-0 data for orbit of $x = 0$ of length $n$ under $T_{\sqrt{2}-1}$ . Highlighted transition times indicate first occurrence of these new transition times. . . . .	18

# **Chapter 1**

## **INTRODUCTION**

Mathematics has been classified with the trivializing generalization as the study of patterns. It is true that just beyond this philosophical description is a myriad of mathematical techniques, objects, and results which exhibit those most beautiful forms of symmetry and pattern. Time and time again the exploitation and observation of patterns has lead to both discovery and proof. While this is true in all areas of mathematics there is no greater source of examples than dynamical systems. In this paper we will utilize a tool for visualization to explore the structure of several dynamical systems. In Section 2 we introduce this tool, known as persistent homology, exploring its origins and intended applications. Section 3 applies PH to a discrete dynamical system closely related to classical number theory. In Section 4 we analyze a coupled system of PDEs which model the surface of a binary material as it undergoes broad beam ion bombardment. We then define and apply some simple statistics derived from PH to analyze the patterns which form in this model. Finally in Section 5 we describe the inherent limitations of PH and demonstrate a method inspired by dynamical systems theory for improving the tool itself. Thus this paper will not only discuss some beautiful patterns present in a variety of dynamical systems, which we explore by utilizing persistent homology, but it will also provide an opportunity to study the tool itself by applying to it some carefully chosen dynamical systems.

## Chapter 2

### PERSISTENT HOMOLOGY

Understanding the topology of a set carved out by a collection of equations or prescribing some topological characteristics to a set of noisy data motivated the development of persistent homology. At its core this tool is a method of visualizing data which may lie elusively in dimensions greater than three and in particular when that data is only a coarse or noisy sampling of some underlying space. Here this tool is utilized for and beyond its original purpose; said roughly, to describe coarse topological features of data. In our case this data will be generated by dynamical systems.

By its design and intended application the output of persistent homology, that is the strategy of visualization it renders (called a barcode), tends to require interpretation. However we shall see through example that this tool can reveal, for appropriately chosen data, stunning regularity not provisional to the conclusions of a trained eye. In fact persistent homology led us to a rediscovery and new characterization of a well-known and beautiful observation of the distribution of points under irrational rotations of the circle.

While persistent homology may be defined in greater generality we restrict our attention to more easily described building blocks: simplicial complexes.

#### 2.1 Simplicial Homology

**Definition 2.1.1.** Consider a finite set  $A$ . A subset  $S \subset \mathcal{P}(A)$  of the powerset of  $A$  is called an **abstract simplicial complex** if  $s \in S \implies \mathcal{P}(s) \in S$ .  $s$  is called a **simplex** and we say the dimension of  $s$  is  $|s| - 1$ . The dimension of  $S$  is defined to be the maximum dimension over all simplices it contains. (note: the emptyset being a simplex of a simplicial complex is implied if not explicitly written).

For example take

$$A = \{a, b, c, d, e\} \text{ and}$$

$$S = \{\{a, d, e\}, \{a, d\}, \{a, e\}, \{d, e\}, \{a, c\}, \{a\}, \{c\}, \{d\}, \{e\}\}.$$

$S$  is a simplicial complex. For notational convenience, sets are sometimes written as square-free monomials over the alphabet  $A$  (i.e.  $\{a, d, e\} = ade$ ).

This abstract definition has a concrete geometric interpretation which will be invaluable in understanding persistent homology. In essence we think of singleton sets as points (0 dimensional), 2-subsets as edges (1-dimensional), 3-subsets as faces (2 dimensional), etc. Figure 2.1 shows the simplicial complex  $S$  in our example as a geometric figure as well as a higher dimensional complex  $T$  containing (geometrically) a tetrahedron (i.e. a 4-subset). We will prescribe an orientation to the faces by ordering the terms of the monomial. For example the 1-simplex  $ab$  is an edge oriented by its vertices from  $a$  to  $b$  and the 2-simplex  $abc$  is a face oriented by its edges  $a$  to  $b$ ,  $b$  to  $c$ , then  $c$  to  $a$ .

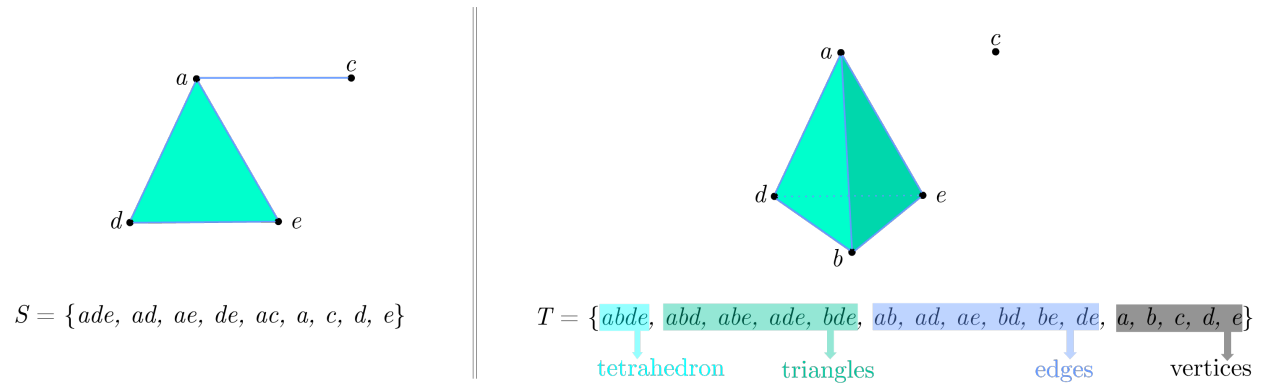


Figure 2.1: Geometric simplicial complexes.

In this way any abstract simplicial complex of dimension  $d$  can be realized as a geometric simplicial complex in  $\mathbb{R}^{2d+1}$ .

*Remark 2.1.1.* With the above examples in mind it is tempting to conclude that the required dimension of the geometric representation in the previous statement is far too generous. But consider the following simplicial complex on five letters:  $\{ab, ac, ad, ae, bc, bd, be, cd, ce, de, a, b, c, d, e\}$ .

This represents the complete graph on five vertices, a non-planar graph which cannot be embedded in  $\mathbb{R}^2$ . In fact Van Kampen and Flores showed that for every dimension  $d$  there is a  $d$ -dimensional simplicial complex which cannot be realized in  $\mathbb{R}^{2d}$  [1].

The definition of a simplicial complex is interpreted in the geometric context in the following way: if an  $n$ -dimensional face (triangle, edge, etc) exists in the complex then so does the  $(n - 1)$ -dimensional boundary of the face (which is itself a collection, generally, of faces).

With simplicial complexes defined we are one step closer to constructing persistent homology. What follows is a series of definitions and remarks to introduce and clarify the additional tools needed.

**Definition 2.1.2.** A **chain complex** (of vector spaces) is a pair  $(V_\bullet, \partial_\bullet)$ , where  $V_\bullet$  is a sequence of vector spaces  $\dots, V_n, V_{n-1}, \dots, V_1, V_0, \dots$  connected by linear transformations  $\partial_n : V_n \rightarrow V_{n-1}$  (called **boundary operators**) with the property that  $\partial_n \circ \partial_{n+1} = 0$  for all  $n$ . A finite collection of vector spaces and boundary maps with the same property is called a **bounded chain complex**.

*Remark 2.1.2.* A chain complex can be defined in greater generality as a sequence of abelian groups. In this context the boundary maps are taken to be homomorphisms. The requirement that composition of successive boundary maps is the 0 map ensures that the image of  $\partial_{n+1}$  is a subspace of the kernel of  $\partial_n$  for all  $n$  which is necessary to define homology. We say a chain complex is **exact** if  $\ker(\partial_n) = \text{im}(\partial_{n+1})$  for all  $n$ .

**Definition 2.1.3.** Let  $(V_\bullet, \partial_\bullet)$  be a chain complex. Define the  $n$ th homology group  $H_n(V_\bullet, \partial_\bullet)$  to be the quotient space of vector spaces <sup>1</sup>

$$H_n(V_\bullet, \partial_\bullet) = \frac{\ker(\partial_n)}{\text{im}(\partial_{n+1})}$$

<sup>1</sup>Had we chosen  $k$ -chains to be formal linear combinations of  $k$ -simplices with integer coefficients, the resulting chain complex would be composed of a sequence of free abelian groups with homology groups being the quotients of the subgroups defined by the kernel mod the image of the appropriate boundary maps.

*Remark 2.1.3.* Notice that every homology group of a chain complex will be trivial if and only if the complex is exact. So homology is thought of as a measurement of the failure of a complex to be exact.

The notions of simplicial complexes and chain complexes are momentarily connected only by their common second word. This is no mere coincidence and the terminology is suggestive of the strong relationship. In fact from a simplicial complex one can construct a chain complex in a natural way.

**Definition 2.1.4.** Let  $S$  be a simplicial complex. For each  $0 \leq k \leq \dim(S)$  define a **simplicial  $k$ -chain** to be a formal sum of  $k$ -dimensional simplices in  $S$  with real coefficients and denote the vector space over the  $k$ -dimensional simplices (whose elements are these formal sums) by  $V_k$ .

To illustrate a  $k$ -chain consider again the example where

$$S = \{ade, ad, ae, de, ac, a, c, d, e\}.$$

There is one 2-dimensional simplex,  $ade$ . We think of it as the basis vector for a 1-dimensional real vector space isomorphic to  $\mathbb{R}$ . Likewise there are four 1-dimensional simplices  $ac, ad, ae$ , and  $de$ . A simplicial 1-chain is a formal sum of the form  $r_1(ac) + r_2(ad) + r_3(ae) + r_4(de)$ ,  $r_i \in \mathbb{R}$ . Together all simplicial 1-chains form a four dimensional real vector space with basis  $\{ac, ad, ae, de\}$ . Finally  $S$  contains four 0-dimensional simplices which define the vector space  $V_0 \cong \mathbb{R}^4$ . It remains to define boundary maps between the vector spaces  $V_\bullet$ .

**Definition 2.1.5.** From the  $n$ -dimensional simplicial complex  $S$  construct the vector spaces  $\{V_n, V_{n-1}, \dots, V_0\}$ . Define the chain complex of  $S$ ,  $(V_\bullet, \partial_\bullet)$  by defining the boundary maps  $\partial_k : V_k \rightarrow V_{k-1}$  on the basis elements of  $V_k$  as follows:

Let  $\sigma = v^0v^1\dots v^k$ . For each  $1 \leq k \leq n$

$$\partial_k(\sigma) = \sum_{i=0}^k (-1)^i v^0 \dots \hat{v^i} \dots v^k$$

where  $v^0 \dots \hat{v^i} \dots v^k = v^0 \dots v^{i-1} v^{i+1} \dots v^k$  (the  $(k-1)$ -simplex derived from the  $k$ -simplex  $\sigma$  by removing the  $i$ th vertex).

It is not difficult to see that  $\partial_k \circ \partial_{k+1} = 0$  for all  $k$  and thus  $(V_\bullet, \partial_\bullet)$  is a bounded chain complex. From this chain complex we define the **simplicial homology** of a simplicial complex as in the general definition of homology:

$$H_k(S) = \frac{\ker(\partial_k)}{\text{im}(\partial_{k+1})}$$

By construction our homology groups will be the quotients of real vector spaces  $\frac{\mathbb{R}^m}{\mathbb{R}^n} \cong \mathbb{R}^{m-n}$ . It is worth noting that the dimension of the resulting vector space is the crucial information contained in the homological data.

**Definition 2.1.6.** The  $k$ th Betti number of a simplicial complex  $S$  is  $\beta_k = \dim(H_k(S))$ .

In general the simplicial homology is very computable, however one would find the computation by hand a painful and tedious process for all but the simplest simplicial complexes. We end this section with such an concrete example. Consider the simplicial complex in Figure 2.2,

$$S = \{abc, ab, ac, bc, ad, cd, a, b, c, d, e\}.$$

We define a chain complex of vector spaces including boundary maps  $\partial_i, 0 \leq i \leq 2$ .

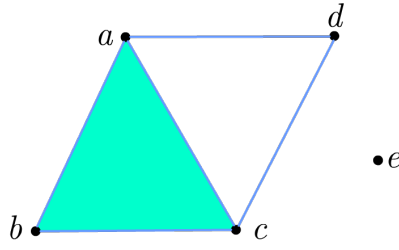
$$V_0 = \langle a, b, c, d, e \rangle = \{r_1a + r_2b + r_3c + r_4d + r_5e | r_i \in \mathbb{R}\} \cong \mathbb{R}^5$$

$$V_1 = \langle ab, ac, bc, ad, cd \rangle = \{s_1ab + s_2ac + s_3bc + s_4ad + s_5cd | s_i \in \mathbb{R}\} \cong \mathbb{R}^5$$

$$V_2 = \langle abc \rangle = \{t_1abc | t_1 \in \mathbb{R}\} \cong \mathbb{R}$$

$$0 \xrightarrow{\partial_3} V_2 \xrightarrow{\partial_2} V_1 \xrightarrow{\partial_1} V_0 \xrightarrow{\partial_0} 0$$

<sup>2</sup>We define  $\partial_0$  to be the 0 map. This convention is used to define homology as opposed to **reduced homology** in which the boundary map between the 0-dimensional simplices and what we will call the (-1)-dimensional simplices (the monomial 1) is defined by the standard definition given. This will have the effect of increasing the dimension of the 0th homology group by one. All other homology groups are unaffected by the choice.



$$S = \{abc, ab, ac, bc, ad, cd, a, b, c, d, e\}$$

Figure 2.2: 2-dimensional simplicial complex.

Now consider how the boundary maps act on basis vectors.  $\partial_0(v) = 0$  for any 0-simplex so by linearity  $\ker(\partial_0) = V_0$ .  $\partial_1(ab) = b - a$ ,  $\partial_1(ac) = c - a$ ,  $\partial_1(bc) = b - c$ ,  $\partial_1(ad) = d - a$ ,  $\partial_1(cd) = c - d$ . Expressed as a matrix this linear transformation is:

$$\partial_1 = \begin{pmatrix} a & b & c & d & e \\ ab & -1 & 1 & 0 & 0 & 0 \\ ac & -1 & 0 & 1 & 0 & 0 \\ ad & -1 & 0 & 0 & 1 & 0 \\ bc & 0 & -1 & 1 & 0 & 0 \\ cd & 0 & 0 & -1 & 1 & 0 \end{pmatrix}$$

The rank of this matrix is 3 and so the dimension of the image of  $\partial_1$  is 3. Thus  $H_0(S) = \frac{\mathbb{R}^5}{\mathbb{R}^3} \cong \mathbb{R}^2$  and the 0th Betti number is  $\beta_0 = 2$ . Similarly we have  $\partial_2(abc) = bc - ac + ab$

$$\partial_2 = \begin{pmatrix} ab & ac & ad & bc & cd \\ abc & 1 & -1 & 0 & 1 & 0 \end{pmatrix}$$

which has with rank 1. By the rank-nullity theorem  $\dim(\ker(\partial_1)) = 5 - 3 = 2$ . Therefore  $H_1(S) = \frac{\mathbb{R}^2}{\mathbb{R}} \cong \mathbb{R}$  and the 1st Betti number is  $\beta_1 = 1$ . All higher order homologies are clearly trivial (i.e. the 0 dimensional vector space consisting of the zero vector).

While this construction appears mysterious, the Betti numbers have very nice geometric interpretations. Roughly speaking  $\beta_0$  is the number of connected components of the sim-

plicial complex,  $\beta_1$  is the number of topological 2-dimensional holes,  $\beta_2$  is the number of 3-dimensional holes (voids) [2]. In our example  $S$  had two connected components as well as a single hole formed by the triangle with edges  $ac$ ,  $ad$ , and  $cd$ . Beyond the significance of the individual Betti numbers it is worth pointing out that homology is a topological invariant. We say a topological space can be triangulated if there exists a homeomorphism between the space and some simplicial complex. A deep theorem of algebraic topology says that the homology the space is independent of choice of triangulation and, furthermore, is homotopy invariant [3].

With simplicial homology established we are ready to introduce persistent homology.

## 2.2 The Rips Complex

The first objects with which we are concerned are finite collections of points of a metric space  $(M, d)$ . If we label such a set of points  $S = \{s_1, \dots, s_n\}$  we can think of these points as vertices in a 0-dimensional simplicial complex. Given the geometric realization of any abstract simplicial complex in the previous section it is not hard to imagine constructing other simplicial complexes from this vertex set. For example imagine connecting an edge between  $s_1$  and  $s_2$  to define a new simplicial complex  $S' = \{s_1s_2\} \cup S$ . Further imagine adding edges  $s_2s_3, s_3s_1$ , and the face  $s_1s_2s_3$  to construct  $S'' = \{s_1s_2s_3, s_2s_3, s_3s_1\} \cup S'$ . Observe that we have created a sequence of simplicial complexes with the property  $S \subset S' \subset S''$ . This is the defining characteristic of persistent homology: a collection of complexes (simplicial or otherwise)  $\{S_i\}_{i \in \mathbb{N}}$  equipped with inclusion maps from  $S_i$  to  $S_{i+1}$ . The fact that these injections induce maps on the homology groups [3] is the property which persistent homology exploits. This is because generators of the homology groups will disappear as our simplexes grow. For example, if one were to do the computation, they would find that  $H_0(S) \cong \mathbb{R}^n$

(generated by the vertices) while  $H_0(S') \cong \mathbb{R}^{n-1}$  since the dimension of the image of  $\partial_1$  becomes a 1-dimensional subspace of  $V_0$  in the simplicial complex  $S'$ .<sup>3</sup>

Notice that such a process must necessarily terminate with the simplicial complex which is the power set of  $S$  (the complex containing all possible simplicial complexes over  $S$ ).

**Definition 2.2.1.** Consider a positive real parameter  $t \in \mathbb{R}^+$ . For each  $t$  define a simplicial complex  $S_t$  on the vertex set  $S_0 := S = \{s_1, \dots, s_n\}$  such that if  $r < t$  then  $S_r \subseteq S_t$  ( $S_r$  is a subcomplex of  $S_t$ ). Then the collection of homology groups  $H_k(S_t)$  is a **persistent homology**.  $t$  is called a **filtration time**.

The purpose for such a construction is to track those topological features which persist for large filtration times and to identify the exact times when changes in the simplicial complexes occur. Notice that since we are taking our collection of points to be finite there will be a finite number of **transition times**; the values of the indexing parameter where a change in the complex occurs.

There are several established and useful persistent homologies, or ways of constructing a collection of complexes satisfying the required inclusion conditions. We restrict ourselves to a very computable and easily described method.

**Definition 2.2.2.** Let  $S_0 := S = \{s_1, \dots, s_n\}$ . For each filtration time  $t \in \mathbb{R}^+$  define the complex  $S_t = \text{Rips}(S, t)$  to be the complex which includes edge  $s_i s_j$  if  $d(s_i, s_j) \leq t$  and include higher dimensional simplices in  $\text{Rips}(S, t)$  if all of its edges are included. This is called the **Rips filtration**.

Clearly  $S_r \subseteq S_t$  if  $r < t$ . Figure 2.3 shows the evolution of simplicial complexes and transition times using the Rips method for an arrangement of points in the plane.

Using the geometric meaning of the simplicial homology data we observe Table 2.1. In words:  $\beta_0$ , being the number of connected components, decreases as edges are added until, at

<sup>3</sup> $V_1$  is trivial for  $S$  while  $V_1$  is isomorphic to  $\mathbb{R}$  generated by the edge  $s_1 s_2$  for  $S'$ .

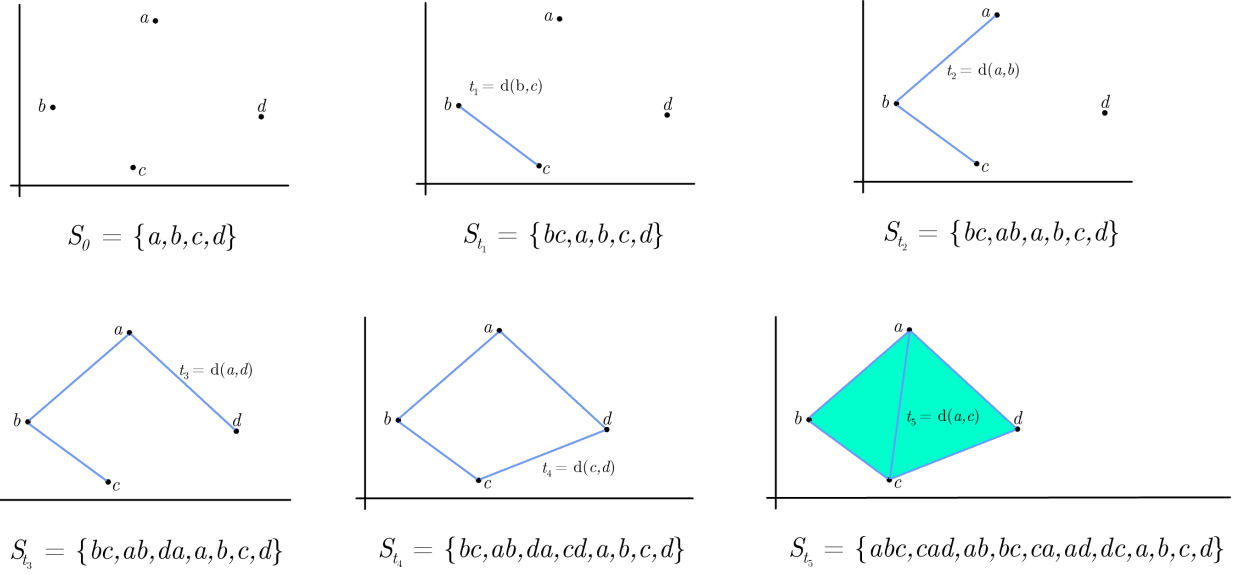


Figure 2.3: Sequence of simplicial complexes using Rips method.

filtration times ( $t$ )	$\beta_0$	$\beta_1$
$0 \leq t < t_1$	4	0
$t_1 \leq t < t_2$	3	0
$t_2 \leq t < t_3$	2	0
$t_3 \leq t < t_4$	1	0
$t_4 \leq t < t_5$	1	1
$t_5 \leq t$	1	0

Table 2.1: Persistent homology data

times greater than  $t_3$ , the complex is one connected component. At time  $t_4$  one hole appears (corresponding to  $\beta_1 = 1$ ) until time  $t_5$  when the two faces are added, filling the hole.

Even with this simple example the amount of information encoded in the persistent homology is cumbersome at best. Also the effective rendering of the complexes is only really possible because the metric space in this example is the plane. However, even in the plane, as the vertex set grows towards something more realistic, visualizing the sequence of complexes and constructing a table of Betti numbers at transition times becomes much less useful.

## 2.3 Barcodes

To solve the problem of storing and interpreting the persistent homology data a method of visualization called a **barcode** is employed. For each  $i, 0 \leq i \leq n$  where  $n$  is the maximum index of the Betti numbers across all simplicial complexes we will construct a Betti- $i$  barcode. For fixed  $i$  we draw a copy of the indexing set (filtration times) along the horizontal axis and at each time  $t$  plot  $\beta_i(S_t)$  many points (along the vertical axis). The result is a series of lines (or bars) which appear and disappear at transition times.

Sometimes (in particular in the Matlab program Plex - used to compute and display barcodes) these are called the dimension-0 and dimension-1 Rips barcodes. However, in that language the dimension- $i$  barcode contains information related to the  $i$ th Betti number, which is the dimension of the  $i$ th homology group. This overuse of the term ‘dimension’ can be a source of confusion, so we will call the barcode associated with the  $i$ th Betti number the Betti- $i$  barcode.

Figure 2.4 shows the Betti-0 and Betti-1 Rips barcodes associated with the four points in the plane in Figure 2.3.

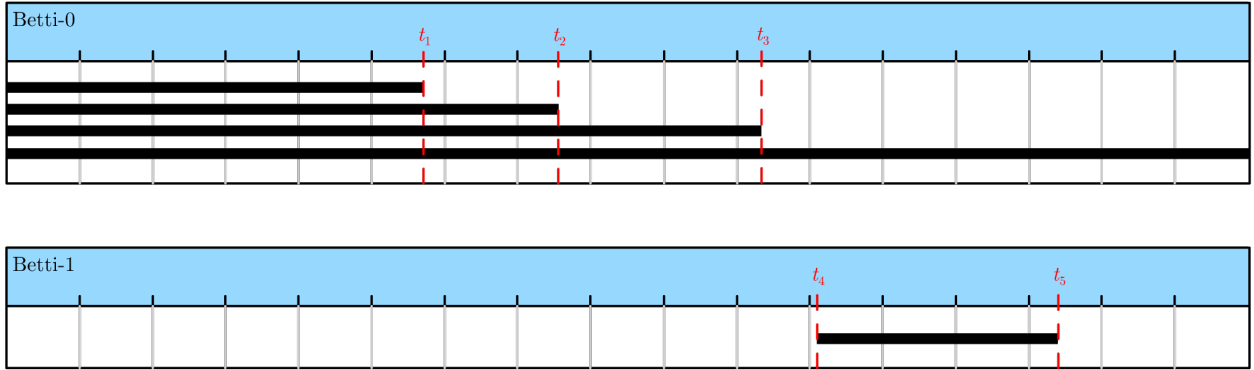


Figure 2.4: Barcodes displaying the transition times where Betti numbers change.

Certainly as we increase the number of points  $n$  in our sample the Betti-0 Rips barcodes can become very large. This reflects the fact that at filtration time  $t = 0$  there are necessarily  $n$  bars since the simplicial complex is merely the set of singletons (the points themselves) and

has  $n$  connected components. Nonetheless this method of visualization provides a reasonably compact way of displaying a huge array of data.

As was stated in the introduction to this section persistent homology is used to try and extract coarse topological information about an underlying set given a rough or noisy sampling; what is sometimes called **point-cloud data**. Such conclusions regarding or descriptions of the underlying set require interpretation of the barcodes and are subject to concerns such as the uniformity and accuracy of the sampling. In our example one might conclude that the four points were sampled from a set that is homeomorphic to a circle since one Betti-1 barcode appears and persists for a relatively long interval before disappearing; suggesting a single hole.

*Remark 2.3.1.* Perhaps more concerning is that the Rips complex can show higher dimensional topological features than can exist in the space from which the points are sampled.<sup>4</sup>

One could instead use the Čech complex which does not present these problems. Consider a set of points  $S_0$  with a metric, then the Čech complex  $S_\epsilon$  will contain an  $n$ -simplex for those subsets of  $n+1$  points which lie in a ball of radius  $\epsilon/2$ . More geometrically consider  $U_\epsilon = \bigcup_{s \in S_0} B_{\epsilon/2}(s)$ ; the union of the balls of radius  $\epsilon/2$  centered on the vertex set  $S_0$ . The Nerve Lemma [4] states that  $U_\epsilon$  is homotopy equivalent to  $S_\epsilon$  which is not true for the Rips filtration. However, the difficulty in computing the Čech complex compared with the highly computable Rips complex and the scope of our first application justifies our use of the latter.

---

<sup>4</sup>As an example consider 17 points evenly distributed around a circle of radius 1. Approximately at filtration time  $t = 1.79$  a Betti-3 barcode appears and persists until  $t = 1.92$  when a Betti-5 barcode appears and persists until  $t = 1.99$ .

## Chapter 3

### THE CIRCLE MAP

The first dynamical system of interest is the well-studied circle map. For a fixed number  $\theta \in (0, 1)$  define  $T_\theta : [0, 1) \rightarrow [0, 1)$  by

$$T_\theta(x) = x + \theta \mod 1$$

We think of this simple version of the circle map as rotation of a circle of circumference 1 by an angle  $\theta$ . It is known that for  $\theta \in \mathbb{R} - \mathbb{Q}$  this map is ergodic (for a proof using Fourier series see [5]). In particular the forward orbit of a point  $x \in (0, 1)$  under iterations of  $T_\theta$  is dense in  $(0, 1)$  for irrational  $\theta$ , while orbits are periodic for rational  $\theta$ . This motivates considering how the dynamics of the circle map are connected to classical number theory.

Another motivation originates from phyllotaxis, the arrangement of leaves on a plant stem. In [6] a modified circle map is defined and its properties are explored. In particular this modified circle map tracks the number of iterations as well as the displacement – becoming a system acting on the plane. The y-axis can be thought of as the time variable while the x-axis tracks the spatial position recorded by the standard circle map. This produces a cylindrical lattice which is then mapped to the disk under an area preserving change of coordinates. The family of lattices is defined in complete generality in [6].

**Definition 3.0.1.**  $\mathbb{L}(\lambda, R, \theta, g) = \left\{ z_1(\lambda, 2\pi R\theta) + z_2(0, \frac{2\pi R}{g}) | (z_1, z_2) \in \mathbb{Z}^2 \right\}$ . Where  $\lambda \in \mathbb{R}^+, g \in \mathbb{N}$  is the  $\frac{2\pi R}{g}$ -periodic lattice in the plane (a cylindrical lattice on a cylinder of radius  $R$ ).

For simplicity we restrict our attention to  $\lambda = g = 1, R = \frac{1}{2\pi}$ . Explicitly  $T_\theta^n(0) = (\{n\theta\}, n) \in \mathbb{R}^2$  with Cartesian coordinates. Mapping the lattice (the orbit of 0 under  $T'_\theta$ ) to the disk under an area preserving transformation defines the modified circle map:

$$(x, y) \mapsto (\sqrt{y} \cos(2\pi x), \sqrt{y} \sin(2\pi x)), \text{ for } (x, y) \in \mathbb{L}(1, \frac{1}{2\pi}, \theta, 1).$$

Orbits under the modified circle map are unbounded and so even for rational  $\theta$  orbits are no longer periodic. However points in the orbit of rational rotations lie on a finite number of rays emanating from the origin. For irrational  $\theta$ , spirals are observed and subtle features of the distribution of points under different choices of rotation angle can be seen<sup>1</sup>. In Figure 3.1 we have purposefully chosen to compare the golden number  $\left\{ \frac{1+\sqrt{5}}{2} \right\}$  (a quadratic algebraic number) with  $\pi$  (a transcendental number) to illustrate this difference in distribution.

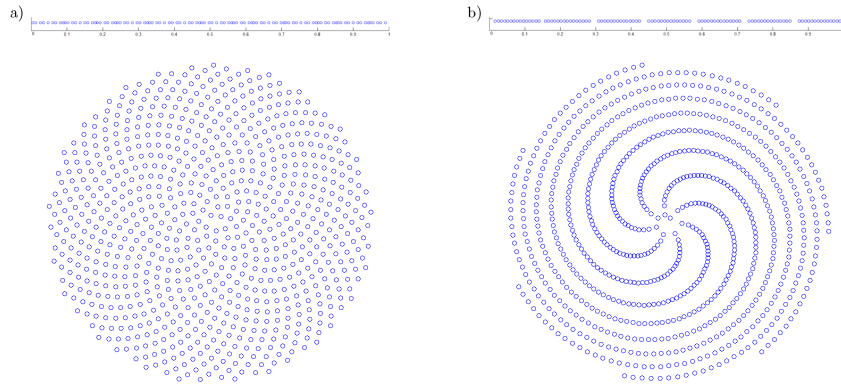


Figure 3.1: 100/800 iterations of the circle/modification circle map with angle a)  $\left\{ \frac{1+\sqrt{5}}{2} \right\}$  and b)  $\pi$ .

Applying a Rips filtration to the orbit of initial condition  $x = 0$  under the modified circle map for different choices of rotation angle reiterates the contrast in the distribution of points, as seen in Figure 3.2.

For now we return our focus to the standard circle map  $T_\theta$  as it will prove sufficient to address some of these observations.

Fix  $\phi = \left\{ 1 + \frac{5}{2} \right\} \approx .61803$  and consider the Betti-0 barcodes of orbits of varying length under iteration  $T_\phi$  (starting at 0). In contrast to the highly irregular and unpredictable barcodes illustrated in Figure 3.2 and in the literature (when this technique is applied to

<sup>5</sup>Notice the 7 clusters of points in the upper plot of Figure 3.1 b) and the 7 distinct spirals in the lower image.

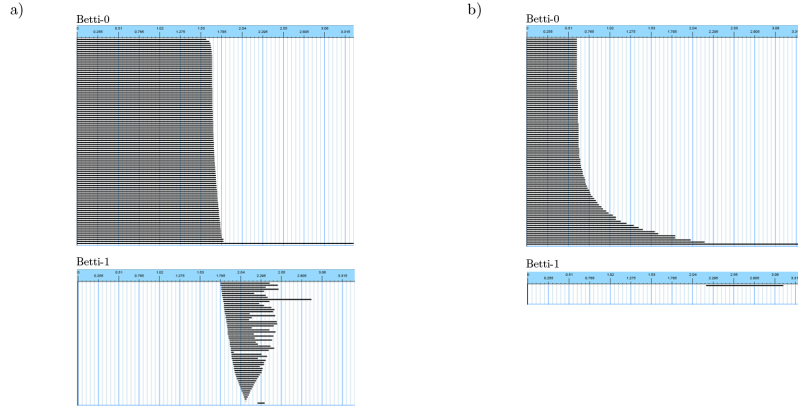


Figure 3.2: Rips barcodes of 100 iterations of the modified circle map with angle a)  $\left\{\frac{1+\sqrt{5}}{2}\right\}$  and b)  $\pi$ .

real-world data) stunning regularity is observed. In Figure 3.3 the Betti-0 barcodes for the plots of  $n = 15, 21, 40, 50$ , and 100 points are given.

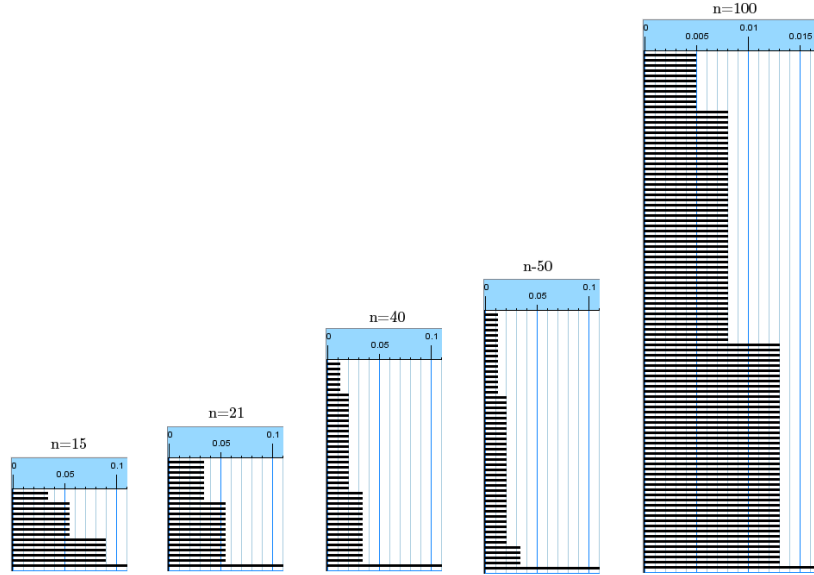


Figure 3.3: Betti-0 barcodes for orbits under  $T_\phi$  of various length

We observe that there are at most 3 transition times where the number of Betti-0 barcodes decreases, with exactly 2 transition times in the plot of 21 points. The regularity in these barcodes goes deeper; for orbits of fixed length in which three transition times are present, the sum of the smaller two transition times is observed to be the third. And, for example, the last transition time for  $n = 40$  is the same as the middle transition time for

$n = 21$ . More to the point a new transition time is introduced when a 22nd point is added. Finally notice that for both  $n = 40$  and  $n = 50$  the simplicial complexes at filtration times between the first and second transition times have 34 connected components. In fact this is true for all  $n$ ,  $34 < n < 55$ . Consider Table 3.1 which records the barcode data for  $n$  points and indicates when a new filtration time is introduced.

no. of points ( $n$ )	$\beta_0$ (transition time)	$\beta_0$ (transition time)	$\beta_0$ (transition time)	new filt. time?
50	34 (.0131556)	5 (.021286)	1 (.0344416)	
51	34 (.0131556)	4 (.021286)	1 (.0344416)	
52	34 (.0131556)	3 (.021286)	1 (.0344416)	
53	34 (.0131556)	2 (.021286)	1 (.0344416)	
54	34 (.0131556)	1 (.021286)		
55	34 (.0131556)	1 (.021286)		
56	55 (.0081306)	33 (.0131556)	1 (.0212862)	new time (smaller)
⋮	⋮	⋮	⋮	⋮
89	55 (.0081306)	1 (.0131556)		
90	89 (.0050249)	53 (.0081306)	1 (.0131556)	new time (smaller)
⋮	⋮	⋮	⋮	⋮
144	89 (.0050249)	1 (.0081306)		
145	144 (.0031056)	88 (.0050249)	1 (.0081306)	new time (smaller)
⋮	⋮	⋮	⋮	⋮

Table 3.1: Betti-0 data for orbit of  $x = 0$  of length  $n$  under  $T_\phi$ . Highlighted transition times indicate first occurrence of these new transition times.

Counting the number of connected components which appear after the first transition time (as we increase the orbit length under  $T_\phi$ ) yields a sequence of integers which are familiar to most: the Fibonacci sequence. The barcodes lengths are significant as well. In particular we observe that in the second column (the smallest filtration time where a transition occurs) the transition time is exactly the distance from  $\beta_0 \cdot \phi$  to the nearest integer. To understand the significance of these integers and these transition times we briefly discuss a few results from classical number theory.

### 3.1 Continued Fractions

There is another dynamical system on the unit interval closely related to the circle map lurking in the background.

**Definition 3.1.1.** The **Gauss Map**  $G : [0, 1) \rightarrow [0, 1)$

$$G(x) = \begin{cases} \left\{ \frac{1}{x} \right\}, & \text{if } x \neq 0 \\ 0, & \text{if } x = 0 \end{cases}$$

This map can be used to construct the continued fraction expansion of any real number.

For  $k \in \mathbb{N}$   $a_k = \left\lfloor \frac{1}{G^k(\theta)} \right\rfloor$ . Then  $\theta = [a_0; a_1, a_2, \dots] = a_0 + \cfrac{1}{a_1 + \cfrac{1}{a_2 + \cfrac{1}{a_3 + \dots}}}$

fraction expansion (CFE) of  $\theta$ . The orbit of the Gauss map is finite if and only if theta is rational, eventually terminating when  $G^m(q) = 0, q \in \mathbb{Q}$  for some  $m$ . Thus the CFE of  $\theta \in \mathbb{R}$  is finite if and only if  $\theta \in \mathbb{Q}$ . Given an irrational number with a non-finite CFE it is natural to consider the sequence of rational numbers given by truncating the continued fraction.

**Definition 3.1.2.** The  $n$ th **partial convergent** of  $\theta = [a_0; a_1, a_2, \dots]$  is the truncated continued fraction  $[a_0; a_1, a_2, \dots, a_n]$ .

**Proposition 3.1.1.** Let  $p_k = a_k p_{k-1} + p_{k-2}; p_0 = a_0, p_1 = a_1 a_0 + 1$  and  $q_k = a_k q_{k-1} + q_{k-2}; q_0 = 1, q_1 = a_1$ . Then  $[a_0; a_1, a_2, \dots, a_n] = \frac{p_n}{q_n}$ .

A proof of this result and a complete treatment of other results referenced here are available in [7] and many other classical number theory texts. For example many statements about the convergence of the partial convergents and how well a number is approximated by its convergents can be made. One rough observation is that larger partial quotients in the CFE of a number will result in faster convergence of partial convergents.

For irrational numbers the algebraic degree tells us more about the dynamics of the Gauss map and thus the rate of convergence of their partial convergents.

**Theorem 3.1.1.** *The continued fraction expansion of  $\theta \in \mathbb{R}$  is periodic iff  $\theta$  is a quadratic surd.*

This statement is as much is as known about the dynamics of the Gauss map on algebraic numbers. For example it is not even known if the partial quotients of the continued fraction

expansion of any degree three algebraic number are bounded or unbounded. We mention this now only because an equivalent characterization of the boundedness of partial quotients will follow from the main result in this section.

Recall the observations at the end of Section 3; the appearance of the Fibonacci sequence in the Betti-0 barcodes. In the language of CF theory these integers are the denominators (and in fact the numerators) of the partial convergents to  $\phi = [0; 1, 1, \bar{1}] = \left\{ \frac{1+\sqrt{5}}{2} \right\}$ . Recall also that when plotting a Fibonacci number of points under rotation by  $\phi$  only two transition times appeared and the addition of a single point (extending the orbit length from 21 to 22 for example) resulted in a single barcode of a new (shorter) length to appear. It is tempting to conclude that this is true for all irrationals but consider the analogous data to Table 3.1 for  $\theta = \{\sqrt{2}\} = [0; 2, 2, \bar{2}]$ , given in Table 3.2.

no. of points ( $n$ )	$\beta_0$ (transition time)	$\beta_0$ (transition time)	$\beta_0$ (transition time)	new filt. time?
7	5 (.071067)	1 (.171572)		
8	5 (.071067)	4 ( <b>.100505</b> )	1 (.171572)	new time (middle)
9	5 (.071067)	3 (.100505)	1 (.171572)	
10	5 (.071067)	2 (.100505)	1 (.171572)	
11	5 (.071067)	1 (.100505)		
12	5 (.071067)	1 (.100505)		
13	12 ( <b>.029437</b> )	4 (.071067)	1 (.100505)	new time (smaller)
⋮	⋮	⋮	⋮	⋮
17	12 (.029437)	1 (.071067)		
18	12 (.029437)	11 ( <b>.04163</b> )	1 (.071067)	new time (middle)
⋮	⋮	⋮	⋮	⋮
29	12 (.029437)	1 (.04163)		
30	29 ( <b>.012193</b> )	11 (.029437)	1 (.04163)	new time (smaller)
⋮	⋮	⋮	⋮	⋮

Table 3.2: Betti-0 data for orbit of  $x = 0$  of length  $n$  under  $T_{\sqrt{2}-1}$ . Highlighted transition times indicate first occurrence of these new transition times.

For  $\{\sqrt{2}\}$  the denominators of the partial convergents are  $\{2, 5, 12, 29, 70, \dots\}$ , while new transition times are introduced immediately after  $n \in \{2, 3, 5, 7, 12, 17, 29, 41, 70, \dots\}$ . The observant will see that new smallest transition time are introduced immediately after the denominators of the partial convergents, while new transition times larger than the smallest existing time but smaller than the largest existing time are introduced at these other special numbers. The subtlety is that partial convergents only tell part of the story. Recall the partial convergents are defined by a recurrence relation involving the partial quotients:

$$q_k = a_k q_{k-1} + q_{k-2}$$

This relation can be expressed by the vector-matrix equation

$$\begin{bmatrix} q_k \\ q_{k-1} \end{bmatrix} = \begin{bmatrix} a_k & 1 \\ 1 & 0 \end{bmatrix} \cdot \begin{bmatrix} q_{k-1} \\ q_{k-2} \end{bmatrix}.$$

Thus one can compute the denominator of the  $k$ th partial convergent by multiplying  $\begin{bmatrix} q_1 \\ q_0 \end{bmatrix}$  on the left by the matrix product  $\begin{bmatrix} a_k & 1 \\ 1 & 0 \end{bmatrix} \dots \begin{bmatrix} a_1 & 1 \\ 1 & 0 \end{bmatrix}$

**Example 3.1.1.**  $\{\sqrt{2}\} = [0; 2, 2, \bar{2}]$ ; ( $a_i = 2, \forall i$ ).

$$\begin{bmatrix} 5 \\ 2 \end{bmatrix} = \begin{bmatrix} 2 & 1 \\ 1 & 0 \end{bmatrix}^1 \cdot \begin{bmatrix} 2 \\ 1 \end{bmatrix} \quad \begin{bmatrix} 12 \\ 5 \end{bmatrix} = \begin{bmatrix} 2 & 1 \\ 1 & 0 \end{bmatrix}^2 \cdot \begin{bmatrix} 2 \\ 1 \end{bmatrix} \quad \begin{bmatrix} 29 \\ 12 \end{bmatrix} = \begin{bmatrix} 2 & 1 \\ 1 & 0 \end{bmatrix}^3 \cdot \begin{bmatrix} 2 \\ 1 \end{bmatrix}$$

Again, the intermediate integers which are associated with the appearance of new transition times are not explicitly derived from the recurrence relation which defines the partial convergents. However, matrices of the form  $\begin{bmatrix} n & 1 \\ 1 & 0 \end{bmatrix}$  can be factored into the product of  $\{0, 1\}$ -matrices. We fix these matrices for the remainder of the discussion with a definition

**Definition 3.1.3.** Let  $F = \begin{bmatrix} 1 & 1 \\ 1 & 0 \end{bmatrix}$  be the **Fibonacci matrix** and  $G = \begin{bmatrix} 1 & 1 \\ 0 & 1 \end{bmatrix}$  the **inner matrix**.

**Proposition 3.1.2.**  $\begin{bmatrix} n & 1 \\ 1 & 0 \end{bmatrix} = G^{n-1} F$

The proof is a straightforward exercise in induction and matrix multiplication.

Now consider multiplication of the vectors  $\begin{bmatrix} q_1 \\ q_0 \end{bmatrix}, \begin{bmatrix} p_1 \\ p_0 \end{bmatrix}$  by the factored forms of the matrices derived from the CFE of some number  $\theta = [a_0; a_1, a_2, \dots]$ . Recording the first entry in the vectors after multiplication by every matrix (either  $F$  or  $G$ ) gives rise to a sequence of integers which contains as a subsequence those integers which are partial convergents to  $\theta$ .

**Definition 3.1.4.** We define the **full sequence of convergents** and call all rational approximates obtained from the full sequence the **total convergents**. We call the sequence of partial convergents the **outer sequence** and those members of the full sequence not in the outer sequence the **inner sequence**.

**Example 3.1.2.**  $\{\sqrt{2}\} = [0; 2, 2, \bar{2}]$ ; ( $a_i = 2, \forall i$ ).

$$\dots G \cdot F \cdot G \cdot F \cdot G \cdot F \cdot [\frac{2}{1}]$$

$$\text{Outer Sequence: } [\frac{2}{1}], \quad [\frac{5}{2}], \quad [\frac{12}{5}], \quad [\frac{29}{12}], \quad [\frac{70}{29}] \dots$$

$$\text{Inner Sequence: } [\frac{3}{2}], \quad [\frac{7}{5}], \quad [\frac{17}{12}], \quad [\frac{41}{29}], \quad \dots$$

$$\text{Full Sequence: } [\frac{2}{1}], [\frac{3}{2}], [\frac{5}{2}], [\frac{7}{5}], [\frac{12}{5}], [\frac{17}{12}], [\frac{29}{12}], [\frac{41}{29}], [\frac{70}{29}] \dots$$

With the full sequence of convergents defined we are ready to state the observations in the Betti-0 barcodes as several conjectures. Let  $\theta \in [0, 1) - \mathbb{Q}$  and consider the orbit of length  $n$  of a point under iterations of the map  $T_\theta$ .

**Conjecture 3.1.1.** There are at most three transition times in the Betti-0 barcode  $0 < d1_k < d2_k < d3_k$  with  $d1_k + d2_k = d3_k$  taking the number of connected components from  $n > n1 > n2 \geq 1$ .

**Conjecture 3.1.2.** The number of connected components in the Rips simplicial complex for filtration times between the first and second transition times is  $q_k$  where  $q_k$  is the largest denominator in the partial convergents to  $\theta$  not exceeding  $n$ .

**Conjecture 3.1.3.** If introducing the  $(n+1)$ th point results in a new transition time which is smaller than the existing two transition times (those in the Betti-0 barcodes for  $n$  points) then  $n = q_k$  for some  $k$  ( $n$  is in the outer sequence). Otherwise (if the new filtration time is in the middle of the existing two) then  $n$  is an element of the inner sequence. Moreover the number of connected components as in conjecture 3.1 remains the same.

The last sentence of conjecture 3.2 illustrates why a transition time being inserted between the existing two filtration times does not change the number of connected components observed after the first transition time. On the other hand a new smallest filtration time (appearing in a plot of  $n+1$  points) will correspond to a single barcode of that length appearing at the top of the Betti-0 barcode. Thus after the first transition time (this new smallest one)

there will be exactly  $n$  connected components, which is the content of this conjecture. If the above conjectures are true the following recursion formula can be given for the smallest (and thus all <sup>2</sup>) the transition times which will appear in the Betti-0 barcodes for a plot of  $n$  points.

**Corollary 3.1.1.** *Let the full sequence of  $\theta$  be the set  $\{n_k\}_{k \in \mathbb{N}}$  and for each  $k$  let  $n1_k$  be the largest element of the outer sequence less than or equal to  $n_k$ . If  $d1_k < d2_k$  are the transition times appearing in the Betti-0 barcodes of  $n_k$  points. Then*

$$d1_{k+1} = \begin{cases} \frac{1-d1_k n_k}{n1_k}, & \text{if } d1_k(n_k + n_{k+1}) > 1 \\ d1_k, & \text{if } d1_k(n_k + n_{k+1}) < 1 \end{cases}$$

*Proof.* Fix  $n \in \mathbb{N}, n > 3$ . From conjecture 3.1.1 we know  $(n-n1)d1 + (n1-n2)d2 + n3d3 = 1$ . If we restrict our attention only to those numbers of points where addition of a single new point under the map  $T_\theta$  causes the creation of a new filtration time (namely the sequence  $n_k$ ) then this equation becomes  $(n_k - n1_k)d1_k + n1_k d2_k = 1 \implies n_k d1_k + n1_k(d2_k - d1_k) = 1$ . Of course if we have plotted  $n_k$  points and there are only two transition times in the Betti-0 barcode then by the construction of the Rips complex there are only two different distances between any two consecutive points. Implicit in conjecture 3.1.1 and 3.1.3 (and the reason for the behavior of the rotation map) is that the introduction of the  $n_k + 1$  point will split the largest of these two gaps into two smaller gaps. There are only two possibilities for the resulting gap: Either the existing smaller gap remains the smallest gap (i.e.  $d1_{k+1} = d1_k$ ) which happens when  $d1_k(n_k + n_{k+1}) < 1$  or the new gap is smaller than any previously seen (i.e.  $d1_{k+1} < d1_k$ ) which implies that  $d1_{k+1} = d2_k - d1_k$  by conjecture 3.1.1. This occurs when  $d1_k(n_k + n_{k+1}) > 1$ .  $\square$

---

<sup>2</sup> $d2_k = \frac{1-(n_k - n1_k)d1_k}{n1_k}$

It remains then to prove conjectures 3.1.1-3.1.3. As it happens the content of the above conjectures (which we observed through an application of the, perhaps overly sophisticated, tool of persistent homology) is known by the name of the Steinhaus Conjecture which was proved over 50 years ago and was given the name the Three Gap/Theorem.

**Theorem 3.1.2.** (*The Three Gap/Theorem*) Fix  $\theta = [a_0; a_1, a_2, \dots]$ . Every integer  $n \geq 1$  can be written uniquely as  $n = mq_k + q_{k-1} + r$  where  $1 \leq m \leq q_{k+1}$  and  $0 \leq r \leq q_k$ . For  $n+1$  points placed by rotations by  $\theta$ , there are:

$n+1 - q_k$  gaps between successive points of length  $d1_k$ ,

$r+1$  gaps between successive points of length  $d2_k$ , and

$q_k - r - 1$  gaps between successive points of length  $d3_k$

To illustrate the connection between this theorem and the discussion above consider the following example where the dataset is

$$\{T_{\sqrt[3]{2}}^i(0) | i = 0, 1, \dots, n-1 = 16\}$$

**Example 3.1.3.** We consider the first 17 points in the forward orbit of the point 0 under rotation by  $T_{\sqrt[3]{2}}$ , ( $\sqrt[3]{2} = [1; 3, 1, 5, 1, 1, 4, \dots]$ ). Figure 3.4 shows the Betti-0 barcode produced by the Rips filtration applied to this collection of points in the plane. Using the notation in Theorem 3.1.2 we have  $16 = n = mq_k + q_{k-1} + r$ . Here  $k = 2$ , (corresponding to  $a_3 = 5$ ) and one can calculate from the above partial quotients  $q_2 = 4$ . Then  $r = 1, m = 3$  are the only values satisfying the conditions of the theorem. Thus our expression for  $n$  becomes  $16 = 3 \cdot 4 + 3 + 1$ .

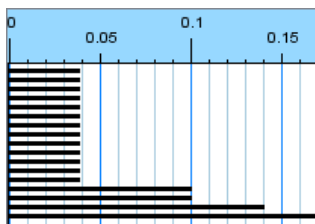


Figure 3.4: Betti-0 barcode produced from the the first 17 points in the forward orbit of 0 under  $T_{\sqrt[3]{2}}$ .

---

17 to 4 connected components  $\longleftrightarrow n + 1 - q_k = 16 + 1 - 4 = 13$   
at the first transition time corresponding to 13 edges (of length  $d_{1k}$ ) being added.

4 to 2 connected components at  $\longleftrightarrow r + 1 = 1 + 1 = 2$   
the second transition time corresponding to 2 edges (of length  $d_{2k}$ ) being added.

The addition of 2 edges at the  $\longleftrightarrow q_k - r - 1 = 4 - 1 - 1 = 2$   
third transition time creates a simplex with a single connected component.

---

Of course the proof of the three distance theorem does not rely on tools of computational algebraic geometry (far from it). However, the novel application of these tools has not only led us to rediscover a beautiful observation about the dynamics of circle maps, but has also provided us with an example which challenges the limitations of the intended scope of the tool. Here the number and the length of the barcodes are not mere artifacts of noisy sampling; a signal which may or may not be clear to the interpreter. Rather the barcodes encode essential information about the nature of the angle of rotation and its continued fraction expansion.

The scope of persistent homology is further broadened by observing that in this application the dataset is not a fixed, noisy sample. It is not even a highly accurate (but nonetheless fixed) sample of points which satisfy some set of equations. Instead, the key to rediscovering the Steinhaus Conjecture was considering the way in which the barcodes changed as points were added by iterations of a dynamical system.

For a moment consider the circle map  $T_\theta$  as acting on the unit circle in the complex plane centered at the origin. In this characterization the orbit of, say  $1 \in \mathbb{C}$ , is dense in the unit circle. As we add points and compute Betti-0 and Betti-1 barcodes we expect the Betti-1 barcode to converge to a single bar starting at filtration time  $t = 0$  and ending at filtration time  $t = 2$  (when every pair of points, including antipodal points, have been connected by an edge). Thus Section 3 provides an opportunity to define a notion of the

evolution, and ultimately the convergence, of barcodes. Such notions could have implications in classifying topologically strange objects such as fractal Julia sets of complex polynomials and in developing a definition of a measure of the degree of ergodicity of the circle map.

We consider another opportunity to analyze the evolution of barcodes in the next section.

## Chapter 4

### ION BOMBARDMENT

Experimental physicists have observed spontaneous pattern formation when a solid surface is bombarded with a broad ion beam [9]-[12]. These patterns vary from parallel ripples to highly ordered hexagonal arrays of nanodots. While academic interest in pattern and defect formation has motivated research, much interest in these experimental observations lies in their potential to improve fabrication of nanostructures or provide effective alternatives to traditional fabrication methods. Ion bombardment has the potential to be a fast method of producing regular nanostructures which are on the order of tens of nanometers; a scale which matches that achieved by modern lithography techniques.

Several competing theories have emerged to model the hexagonal pattern formation observed in experiments; two of which attempt to model the scenario of bombardment of an elemental material [13]-[14] and one (the Bradley/Shipman theory studied in detail in this paper) which emphasizes the necessity of a binary solid in the formation of hexagonal patterns [15]. The first two theories study the Kuramoto-Sivashinsky equation<sup>1</sup>. The latter argues that (generally) within a binary material one material is preferentially sputtered<sup>2</sup> and that this results in a change in the relative concentrations of the two atomic species at the surface. The theory suggests that this change in surface stoichiometry, when coupled with the change in surface topography, is crucial in the formation of hexagonal arrays of nanodots [15].

Naturally one of the primary goals of researchers in this area is to identify parameter values which result in defect-free pattern formations. It is towards this end that we apply

---

<sup>1</sup>Modified with the addition of one or two nonlinear terms

<sup>2</sup>The effect of ejecting atoms from a solid by bombarding the surface with energetic particles.

persistent homology to ion bombardment data, both experimental and simulated. We do so not only in the hope of supporting the models with a new method of comparison, but also to demonstrate another application in which the evolution of barcodes can be studied.

Before we apply the computational homology tools we briefly explore the Bradley/Shipman theory and perform an analysis of the coupled system of equations. In [15] coupled equations of motion describing the surface height and the relative concentrations of the components of the binary material under normal incidence ion bombardment are derived and analyzed. Here we perform a similar treatment of the equations modeling off-normal incidence ion bombardment which introduces an anisotropy in the coupled system. In particular we consider the following system:

$$u_t = \phi - (r_1 u_{xx} + u_{yy}) - \nabla^2 \nabla^2 u + \lambda(r_3 u_x^2 + u_y^2) \quad (4.1)$$

and

$$\phi_t = -a\phi + b(r_2 u_{xx} + u_{yy}) + c\nabla^2 \phi + \nu\phi^2 + \eta\phi^3, \quad (4.2)$$

where  $u(x, y, t)$  is the surface height and  $\phi(x, y, t)$  is the relative concentration of material species. Thus choosing  $\phi = 0$  (and  $b = 0$ ) this system reduces to the anisotropic Kuramoto-Sivashinsky (AKS) equation [20].

$$u_t = -(r_1 u_{xx} + u_{yy}) - \nabla^2 \nabla^2 u + \lambda(r_3 u_x^2 + u_y^2). \quad (4.3)$$

Choosing  $r_1 = r_2 = r_3 = 1$  reduces our system to the normal incidence equations in [15].

In [20] it is predicted that remarkably defect-free ripples can be produced by ion bombardment of a binary material because of the coupling between surface height and composition; an interaction not present during bombardment of an elemental material. The authors compare the AKS equation to the coupled system given in Eqns. 4.1, and 4.2, and illustrate that the high degree of order is not present in the former. In the following sections

we provide a standard analysis of the coupled equations of motions before comparing the models through the lens of PH.

#### 4.1 Linear Stability Analysis

In this section we will perform linear stability analysis about the steady-state solution  $u = \phi = 0$ . First we fix the following notational conventions:  $l^2 := r_1 k_x^2 + k_y^2$  and  $m^2 := r_2 k_x^2 + k_y^2$ , where  $\vec{k} = (k_x, k_y)$ ,  $b_c(\vec{k})$  is the maximum value of  $b$  for which  $\sigma(\vec{k}) = 0$ ,  $b_T = \max_{\vec{k}} b_c(\vec{k})$ , *c.c.* denotes complex conjugate, and  $\Delta_i = r_i \frac{\partial^2}{\partial x^2} + \frac{\partial^2}{\partial y^2}$  for  $i = 1, 2, 3$ .

The linear terms in Eqns. 4.1 and 4.2 can be expressed as a matrix equation;

$$\frac{\partial}{\partial t} \begin{pmatrix} u \\ \phi \end{pmatrix} = \begin{pmatrix} \Delta_1 - \nabla^2 \nabla^2 & 1 \\ b(\Delta_2) & c \nabla^2 - a \end{pmatrix} \begin{pmatrix} u \\ \phi \end{pmatrix}. \quad (4.4)$$

Assuming seperable solutions of the form  $\tilde{u} = u_0 e^{i\vec{k} \cdot \vec{x}} e^{\sigma t}$  and  $\tilde{\phi} = \phi_0 e^{i\vec{k} \cdot \vec{x}} e^{\sigma t}$  (where  $\vec{k} = (k_x, k_y)$ , and  $\vec{x} = (x, y)$ ), and substituting into Eqn. 4.4 gives

$$\sigma \tilde{u} = \tilde{u} r_1 k_x^2 + \tilde{u} k_y^2 - \tilde{u} (\vec{k} \cdot \vec{k})^2 + \tilde{\phi}, \quad (4.5)$$

and

$$\sigma \tilde{\phi} = -a \tilde{\phi} - b(r_2 \tilde{u} k_x^2 + \tilde{u} k_y^2) - c \tilde{\phi} \vec{k} \cdot \vec{k}. \quad (4.6)$$

Then the dispersion relation  $\sigma$  can be seen as the solutions to the eigenvalue problem

$$\sigma \begin{pmatrix} \tilde{u} \\ \tilde{\phi} \end{pmatrix} = \begin{pmatrix} r_1 k_x^2 + k_y^2 - k^4 & 1 \\ -b(r_2 k_x^2 + k_y^2) & -a - ck^2 \end{pmatrix} \begin{pmatrix} \tilde{u} \\ \tilde{\phi} \end{pmatrix}. \quad (4.7)$$

At  $b = b_c(\vec{k})$  (for  $\vec{k} \neq \vec{0}$ ),

$$\begin{pmatrix} -k^4 - l^2 & 1 \\ -b_c(\vec{k})m^2 & -ck^2 - a \end{pmatrix} \begin{pmatrix} 1 \\ k^4 - l^2 \end{pmatrix} = \begin{pmatrix} 0 \\ 0 \end{pmatrix}. \quad (4.8)$$

For  $\vec{k} = \vec{0}$ ,

$$\begin{pmatrix} 0 & 1 \\ 0 & -a \end{pmatrix} \begin{pmatrix} u_0 \\ 0 \end{pmatrix} = \begin{pmatrix} 0 \\ 0 \end{pmatrix}. \quad (4.9)$$

Eqns. 4.8 and 4.9 lead to left eigenvectors,  $v_1 = (ck^2 + a, 1)$  and  $v_2 = (a, 1)$  respectively.

These will be used in the nonlinear analysis in Section 4.1.

Eqn. 4.7 has solutions  $\sigma_{\pm}(k_x, k_y) = \frac{T}{2} \pm \sqrt{\frac{T^2}{4} - D}$ , where

$$\begin{aligned} T &= r_1 k_x^2 + k_y^2 - k^4 - a - ck^2 \\ D &= (r_1 k_x^2 + k_y^2 - k^4)(-a - ck^2) + b(r_2 k_x^2 + k_y^2). \end{aligned} \quad (4.10)$$

Restricting our attention  $\sigma_+$ , we look for unstable wave vectors  $\vec{k} = (k_x, k_y)$  where the dispersion relation is positive. By imposing the condition that  $\sigma = \frac{\partial \sigma}{\partial x} = \frac{\partial \sigma}{\partial y} = 0$  and  $k_x \neq 0$  and  $k_y \neq 0$ , we derive the following equations:

$$\begin{aligned} (a + ck^2) + c(r_1 k_x^2 + k_y^2) - 2k^2(a + ck^2) - ck^4 - b &= 0 \\ r_1(a + ck^2) + c(r_1 k_x^2 + k_y^2) - 2k^2(a + ck^2) - ck^4 - br_2 &= 0 \\ (a + ck^2)(r_1 k_x^2 + k_y^2) - (a + ck^2)k^4 - b(r_2 k_x^2 + k_y^2) &= 0. \end{aligned} \quad (4.11)$$

These equations reduce to

$$\begin{aligned} b \frac{r_2 - 1}{r_1 - 1} &= a + ck^2 \\ k^2 = k_x^2 + k_y^2 &= \frac{r_2 - r_1}{r_2 - 1}. \end{aligned} \tag{4.12}$$

Assuming separately that  $k_y = 0$  and  $k_x = 0$  leads, respectively, to

$$\begin{aligned} br_2 &= r_1(a + ck_x^2) - (a + ck_x^2)k_x^2 \\ k_x^2 &= \frac{cr_1 - a}{2c} \end{aligned} \tag{4.13}$$

$$\begin{aligned} b &= a + ck_y^2 - (a - ck_y^2)k_y^2 \\ k_y^2 &= \frac{c - a}{2c}. \end{aligned} \tag{4.14}$$

This derivation gives critical values of  $b$  :  $b_{T,x} := \frac{(cr_1+a)^2}{4cr_2}$ ,  $b_{T,y} := \frac{(c+a)^2}{4c}$ , and  $b_T := \frac{r_2-1}{r_1-1} \left( a + c \frac{r_2-r_1}{r_2-1} \right)$  in terms of the other parameters.

For fixed choices of these parameters, one or more of the critical values of  $b$  is largest among the three, and as  $b$  is decreased below this critical value, the dispersion relation attains positive values. More precisely if we fix  $a, c, r_1$ , and  $r_2$   $\text{Re}(\sigma_+(\vec{k})) < 0$  for all  $\vec{k}$  if  $b > b_c$  ( $c \in \{x, y, T\}$ ). When  $b = b_c$ ,  $\text{Re}(\sigma_+(\vec{k})) = 0$  for certain wave vectors  $\vec{k}$  (see Eqns. 4.12, 4.13, and 4.14) and is negative elsewhere. As we decrease  $b$  below critical, small regions of unstable wave vectors (i.e.  $\vec{k}$  for which  $\text{Re}(\sigma_+(\vec{k})) > 0$ ) form. Notice that each bifurcation is valid only for certain choices of  $c$  and  $a$ . For example  $b_{T,y}$  requires the critical wavevector to be  $k_y^2 = \frac{c-a}{c}$  which forces  $c > a$ . Figure 4.1 shows regions in the  $ac$ -plane where the various critical values of  $b$  can be present and the prototypical regions of unstable wavevectors associated to each bifurcation.

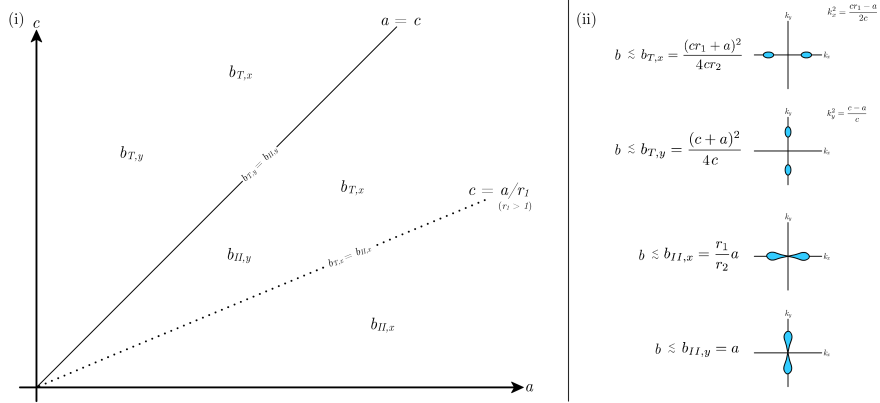


Figure 4.1: (i) The  $ac$ -plane partitioned into regions based on the types of bifurcations which can occur. For example above the line  $a = c$ , either  $b_{T,x}$  or  $b_{T,y}$  will be the critical value of  $b$  (depending on which is larger). On the line  $a = c$  we have  $b_{T,y} = a =: b_{II,y}$  and below the  $a = c$  line  $b_{T,y}$  is no longer valid; here either  $b_{T,x}$  or  $b_{II,y}$  will be the critical value of  $b$  (depending on which is larger). Similar reasoning shows a transition along the  $c = \frac{a}{r_1}$  line, which can be above or below the  $a = c$  line depending on the choice of  $r_1$ . (ii) The prototypical regions where  $\text{Re}(\sigma_+(\vec{k})) > 0$  associated to the various critical values of  $b$ .

For certain choices of parameter values we can force the instability and, for example, a roll pattern to orient itself along the  $k_x$  or  $k_y$  axis. In particular, either critical value  $b_{T,x}$  or  $b_{T,y}$  can be made largest by an appropriate choice of parameters.

**Example 4.1.1.** Choosing  $r_1 = r_2 =: r$  we observe that for fixed  $a, c > 0$ ,  $b_{T,x}$  is a parabola with minimum at  $r = \frac{a}{c}$ .

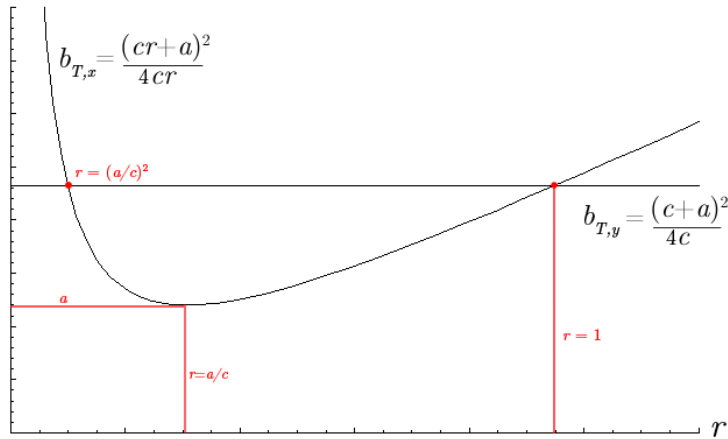


Figure 4.2: Plots of  $b_{T,x}$  and  $b_{T,y}$  as functions of  $r = r_1 = r_2$  showing points and regions of interest.

First,  $k_y^2 = \frac{c-a}{2c}$  forces  $c > a$ . Also for  $b_{T,x}$  to be a valid bifurcation we require  $r \geq \frac{a}{c}$ , thus we restrict our plot to the increasing portion of the curve  $b_{T,x}(r)$ . Equality occurs when  $b_{T,y} = b_{T,x}$  at  $r = 1$  (and  $r = \left(\frac{a}{c}\right)^2 < \frac{a}{c}$  so we ignore it).

As the system is allowed to evolve the solution moves progressively further from the steady state around which our linear analysis was performed ( $u = \phi = 0$ ) and nonlinear terms must be added. In the following section we derive amplitude equations for the time-evolution of the unstable modes which appear for choices of  $b$  below critical.

## 4.2 Non-Linear Analysis

As we have stated, by choosing the parameter  $b$  slightly below critical  $b_T$  the dispersion relation  $\sigma(k_x, k_y)$  is greater than zero for choices of  $\vec{k}$  in some regions of the  $k_x, k_y$ -plane. In the case of normal incidence bombardment the dispersion relation exhibits total rotational invariance and the region of active modes is an annulus. With the introduction of the anisotropy our linear analysis shows that small regions of active modes can appear oriented along the  $k_x$  and/or  $k_y$  axes for certain choices of parameters.

A priori, and in either case, for any choice of  $\epsilon > 0$  there are an infinite number of active modes (for  $a, c$  chosen in Region I). Furthermore the passive modes are not bounded away from 0; in other words there are passive modes which are arbitrarily close to 0. However, since we are searching for solutions which give rise to lattice patterns (rolls, hexagons, etc.) we will assume that all wavevectors contributing to the pattern lie on a lattice [22].

For a hexagonal lattice these wavevectors will be at angles of  $\frac{2\pi}{3}$  to each other. This leads to the resonance:  $\vec{k}_1 + \vec{k}_2 + \vec{k}_3 = \vec{0}$  [22] where we take  $\vec{k}_1$  to be the most unstable mode: corresponding to the maximum value of the dispersion relation. In both normal incidence and off-normal-incidence active modes can resonate through the nonlinear terms in the equations of motion.

We proceed by choosing  $b = b_T(1 - \epsilon b_1)$  for some  $0 < \epsilon \ll 1$  and  $b_1 > 0$  (i.e.  $b$  slightly below critical) and expand our solutions in powers of  $\epsilon$ .

$$\vec{q} = \begin{pmatrix} u \\ \phi \end{pmatrix} = \begin{pmatrix} 0 \\ 0 \end{pmatrix} + \epsilon \vec{q}_1 + \epsilon^2 \vec{q}_2 + \dots, q_j = \begin{pmatrix} u_j \\ \phi_j \end{pmatrix}. \quad (4.15)$$

We also expand the time-derivative in powers of  $\epsilon$ :  $\partial_t = \partial_{\tau_0} + \epsilon \partial_{\tau_1} + \epsilon^2 \partial_{\tau_2} + \dots$ , since the evolution of  $\vec{q}_j$  occurs at a time scale proportional to  $\frac{1}{\epsilon}$ . Define  $\hat{\eta} := \epsilon \eta$ , and assume  $\eta$  is chosen so that  $\hat{\eta}$  is of order 1.

The zeroth order of  $\epsilon$  is trivially  $\begin{pmatrix} 0 \\ 0 \end{pmatrix} = \begin{pmatrix} 0 \\ 0 \end{pmatrix}$ .

The first order of  $\epsilon$  yields

$$\left( \frac{\partial}{\tau_0} - \begin{pmatrix} -\Delta^2 - \Delta_1 & 1 \\ b\Delta_2 & c\Delta - a \end{pmatrix} \right) \begin{pmatrix} u_1 \\ \phi_1 \end{pmatrix} = \begin{pmatrix} 0 \\ 0 \end{pmatrix}. \quad (4.16)$$

From our linear analysis we determined that Eqn. 4.16 has solutions of the form

$$\vec{q}_1 = \begin{pmatrix} u_1 \\ \phi_1 \end{pmatrix} = \sum_{\vec{k} \neq 0} \begin{pmatrix} 1 \\ k^4 - l^2 \end{pmatrix} \left( A_{\vec{k}}(\tau_1) e^{i\vec{k} \cdot \vec{x}} + c.c. \right) + \begin{pmatrix} B \\ 0 \end{pmatrix}, \quad (4.17)$$

where here  $B \in \mathbb{R}$  is called the soft-mode and corresponds to  $\vec{k} = \vec{0}$ .

The second order of  $\epsilon$  leads to

$$\begin{pmatrix} -\Delta^2 - \Delta_1 & 1 \\ b\Delta_2 & c\Delta - a \end{pmatrix} \begin{pmatrix} \epsilon u_1 + \epsilon^2 u_2 \\ \epsilon \phi_1 + \epsilon^2 \phi_2 \end{pmatrix} = -\epsilon^2 \frac{\partial}{\partial \tau_1} \begin{pmatrix} u_1 \\ \phi_1 \end{pmatrix} + \epsilon^2 \begin{pmatrix} \lambda \Delta_3 u_1 \\ \nu \phi_1^2 + \hat{\eta} \phi_1^3 \end{pmatrix}. \quad (4.18)$$

Letting  $L := \begin{pmatrix} -\Delta^2 - \Delta_1 & 1 \\ b\Delta_2 & c\Delta - a \end{pmatrix}$  and equating powers of  $\epsilon$  Eqn. 4.18 reduces to

$$L \begin{pmatrix} u_2 \\ \phi_2 \end{pmatrix} = \frac{1}{\epsilon} L \begin{pmatrix} u_1 \\ \phi_1 \end{pmatrix} - \frac{\partial}{\partial \tau_1} \begin{pmatrix} u_1 \\ \phi_1 \end{pmatrix} + \begin{pmatrix} \lambda \Delta_3 u_1 \\ \nu \phi_1^2 + \hat{\eta} \phi_1^3 \end{pmatrix}. \quad (4.19)$$

Letting  $L_c(\vec{k}) := \begin{pmatrix} -\Delta^2 - \Delta_1 & 1 \\ b_c(\vec{k})\Delta_2 & c\Delta - a \end{pmatrix}$ , note that for each  $\vec{k}$

$$L_c(\vec{k}) \begin{pmatrix} 1 \\ k^4 - l^2 \end{pmatrix} e^{i\vec{k}\cdot\vec{x}} = \begin{pmatrix} 0 \\ 0 \end{pmatrix}, \quad (4.20)$$

which implies that

$$\begin{aligned} L \begin{pmatrix} u_1 \\ \phi_1 \end{pmatrix} &= (L - L_c) \begin{pmatrix} u_1 \\ \phi_1 \end{pmatrix} \\ &= \begin{pmatrix} 0 & 0 \\ (b - b_c(\vec{k}))\Delta_2 & 0 \end{pmatrix} \begin{pmatrix} u_1 \\ \phi_1 \end{pmatrix}. \end{aligned} \quad (4.21)$$

Therefore we can rewrite Eqn. 4.19 as

$$\vec{q}_2 = L \begin{pmatrix} u_2 \\ \phi_2 \end{pmatrix} = \sum_{\vec{k} \in \mathcal{A}} \left( \begin{array}{c} -\frac{\partial}{\partial \tau_1} A_{\vec{k}}(\tau_1) e^{i\vec{k}\cdot\vec{x}} + \lambda \left( r_3 \frac{\partial u_1}{\partial x}^2 + \frac{\partial u_1}{\partial y}^2 \right) \\ \frac{1}{\epsilon} (b - b_c(\vec{k})) \left( r_2 \frac{\partial^2 A_{\vec{k}} e^{i\vec{k}\cdot\vec{x}}}{\partial x^2} + \frac{\partial^2 A_{\vec{k}} e^{i\vec{k}\cdot\vec{x}}}{\partial y^2} \right) - \frac{\partial}{\partial \tau_1} (k^4 - l^2) A_{\vec{k}}(\tau_1) e^{i\vec{k}\cdot\vec{x}} + \nu \phi_1^2 + \hat{\eta} \phi_1^3 \end{array} \right). \quad (19)$$

At this point we take a moment to recall a result from functional analysis:

**Theorem 4.2.1.** (*Fredholm Alternative*) Let  $L : V \rightarrow V$  be a linear map on a Banach space  $V$  and for  $u \in V$  consider the equation  $L(u) = 0$ . Either

- (i)  $L(u) = 0$  has no nontrivial solutions, or
- (ii)  $L^*(v) = 0$  has a nontrivial solution  $v \neq 0$  and  $L(u) = f$  has a solution iff  $\langle v|f \rangle = \langle f|v \rangle = 0$  for all  $v$  such that  $L^*(v) = 0$ .<sup>3</sup>

We also note that  $\int_{\Omega} e^{i\vec{k} \cdot \vec{x}} dA = 0$  for  $\vec{k} \neq \vec{0}$  so that for  $v = \langle v_x, v_y \rangle e^{i\vec{k} \cdot \vec{x}}$  and  $u = \langle u_x, u_y \rangle^T e^{i\vec{j} \cdot \vec{x}}$  we have  $\langle v|u \rangle = 0$  unless  $\vec{k} = \vec{j}$ . Thus for Eqn. 19 to be solvable we require that for every term of the form  $v_{\vec{k}} e^{i\vec{k} \cdot \vec{x}}$ ,  $\vec{k} \neq \vec{0}$ , on the right hand side of Eqn. 19 the vector  $v_{\vec{k}}$  must be orthogonal to the left eigenvector derived in Section 4.1,  $(ck^2 + a, 1)$ .

We apply the solvability condition  $\langle \vec{v}_i | \vec{q}_2 \rangle = 0$ , ( $i = 1, 2$ ) where  $v_1 = (ck^2 + a, 1)$  and  $v_2 = (a, 1)$ , the left eigenvectors corresponding to  $b = b_c(\vec{k})$  and  $\vec{k} = (0, 0)$  respectively.<sup>4</sup>

First let us consider the soft mode. We search for all terms in  $\vec{q}_2$  which involve  $e^{i\vec{0} \cdot \vec{x}}$ . Consider first the terms in the quadratic nonlinearity  $\lambda \left( r_3 \frac{\partial u_1}{\partial x}^2 + \frac{\partial u_1}{\partial y}^2 \right)$ .

$$\begin{aligned} \frac{\partial u_1}{\partial x} = & A_1(i k_{1x}) e^{i \vec{k}_1 \cdot \vec{x}} - A_1^*(i k_{1x}) e^{-i \vec{k}_1 \cdot \vec{x}} \\ & + A_2(i k_{2x}) e^{i \vec{k}_2 \cdot \vec{x}} - A_2^*(i k_{2x}) e^{-i \vec{k}_2 \cdot \vec{x}} \\ & + A_3(i k_{3x}) e^{i \vec{k}_3 \cdot \vec{x}} - A_3^*(i k_{3x}) e^{-i \vec{k}_3 \cdot \vec{x}} \end{aligned} \quad (4.22)$$

<sup>3</sup> $L^*$  is the adjoint of  $L$  and for our purposes  $\langle v|f \rangle = \frac{1}{\Omega} \int_{\Omega} \bar{v} \cdot f dA$  for  $\Omega = [0, 2pi/|k|] \times [0, 2pi/|k|]$ .

<sup>4</sup>While we have derived these equations in complete generality we recall that the wavevectors of interest are  $\vec{k}_1$ , the most unstable mode, and  $\vec{k}_2$  and  $\vec{k}_3$  satisfying  $\vec{k}_1 + \vec{k}_2 + \vec{k}_3 = \vec{0}$ .

$$\begin{aligned} \frac{\partial u_1}{\partial x}^2 = & (\cdots - 2A_1(ik_{1x})e^{i\vec{k}_1 \cdot \vec{x}} A_1^*(ik_{1x})e^{-i\vec{k}_1 \cdot \vec{x}} + \cdots \\ & \cdots - 2A_2(ik_{2x})e^{i\vec{k}_2 \cdot \vec{x}} A_2^*(ik_{2x})e^{-i\vec{k}_2 \cdot \vec{x}} + \cdots \\ & \cdots - 2A_3(ik_{3x})e^{i\vec{k}_3 \cdot \vec{x}} A_3^*(ik_{3x})e^{-i\vec{k}_3 \cdot \vec{x}} + \cdots). \end{aligned} \quad (4.23)$$

A similar equation is derived for  $\frac{\partial u_1}{\partial y}^2$  and the observation is that the only terms in the quadratic nonlinearity  $\lambda \left( r_3 \frac{\partial u_1}{\partial x}^2 + \frac{\partial u_1}{\partial y}^2 \right)$  which involve  $e^{i\vec{0} \cdot \vec{x}}$  are terms involving  $A_j A_j^*$ . The same is true in the quadratic nonlinearity  $\nu \phi_1^2$ :

$$\begin{aligned} \nu \phi_1^2 = & (\cdots + 2(k_1^4 - l_1^2)^2 A_1 A_1^* + \cdots \\ & (\cdots + 2(k_2^4 - l_2^2)^2 A_2 A_2^* + \cdots \\ & (\cdots + 2(k_3^4 - l_3^2)^2 A_3 A_3^* + \cdots). \end{aligned} \quad (4.24)$$

The condition that  $\vec{k}_1 + \vec{k}_2 + \vec{k}_3 = \vec{0}$  forces those terms in the cubic nonlinearity which involve  $A_1 A_2 A_3$  or  $A_1^* A_2^* A_3^*$  to resonate with the soft mode. Therefore

$$\begin{aligned} \hat{\eta} \phi_1^3 = & \hat{\eta} (\cdots + 6(k_1^4 - l_1^2) A_1 (k_2^4 - l_2^2) A_2 (k_3^4 - l_3^2) A_3 + \cdots \\ & \cdots + 6(k_1^4 - l_1^2) A_1^* (k_2^4 - l_2^2) A_2^* (k_3^4 - l_3^2) A_3^* + \cdots), \end{aligned} \quad (4.25)$$

where  $l_i^2 = r_2(k_{ix})^2 + (k_{iy})^2$  ( $i = 1, 2, 3$ ).

Putting the relevant terms together with the solvability condition implies that

$$\begin{aligned} 0 = & (a) \left( -\frac{\partial B}{\partial \tau_1} + 2\lambda \sum_{j=1}^3 [r_3(k_{jx}^2 + (k_{jy}^2) A_j A_j^*] \right) \\ & + (1) \left( 2\nu \sum_{j=1}^3 [(k_j^4 - l_j^2)^2 A_j A_j^*] + 6\hat{\eta}(k_1^4 - l_1^2)(k_2^4 - l_2^2)(k_3^4 - l_3^2)[A_1 A_2 A_3 + A_1^* A_2^* A_3^*] \right) \end{aligned} \quad (4.26)$$

$\implies$

$$\begin{aligned}\frac{\partial B}{\partial \tau} = & \frac{2}{a} \sum_{j=1}^3 (\lambda (r_3(k_{jx}^2) + (k_{jy})^2) + \nu(k_j^4 - l_j^2)) A_j A_j^* \\ & + \frac{6\eta}{a} (k_1^4 - l_1^2)(k_2^4 - l_2^2)(k_3^4 - l_3^2)[A_1 A_2 A_3 + A_1^* A_2^* A_3^*].\end{aligned}\quad (4.27)$$

We next apply the solvability condition to the triad of wavevectors  $\vec{k}_1$ ,  $\vec{k}_2$ , and  $\vec{k}_3$ . Restricting our attention to the amplitude  $A_1$ <sup>5</sup> we first search for terms which involve  $e^{i\vec{k}_1 \cdot \vec{x}}$ . The condition that  $\vec{k}_1 + \vec{k}_2 + \vec{k}_3 = \vec{0} \implies \vec{k}_1 = -\vec{k}_2 - \vec{k}_3$  (similarly  $\vec{k}_2 = -\vec{k}_1 - \vec{k}_3$  and  $\vec{k}_3 = -\vec{k}_1 - \vec{k}_2$ ). In the quadratic nonlinearities  $\lambda \left( r_3 \frac{\partial u_1}{\partial x}^2 + \frac{\partial u_1}{\partial y}^2 \right)$  and  $\nu \phi_1^2$  these are the cross terms containing  $A_2^* A_3^*$ . The cubic nonlinearity contains terms which resonate with  $\vec{k}_1$ , namely those which contain  $A_1 A_i A_i^*$ , ( $i = 1, 2, 3$ ). Then the solvability condition is given by the equation

$$\begin{aligned}0 = & (ck_1^2 + a) \left( -\frac{\partial A_1}{\partial \tau_1} + 2\lambda (r_3(k_{2x} k_{3x}) + (k_{2y} k_{3y}) A_2^* A_3^*) \right) \\ & - \frac{1}{\epsilon} (b - b_c(\vec{k}_1)) (r_2(k_{1x})^2 + (k_{1y})^2) A_1 + (k_1^4 - l_1^2) \frac{\partial A_1}{\partial \tau_1} + 2\nu(k_2^4 - l_2^2)(k_3^4 - l_3^2) A_2^* A_3^* \\ & + 3\hat{\eta} ((k_1^4 - l_1^2)^3 |A_1|^2 + 2(k_1^4 - l_1^2)(k_2^4 - l_2^2)^2 |A_2|^2 + 2(k_1^4 - l_1^2)(k_3^4 - l_3^2)^2 |A_3|^2) A_1\end{aligned}\quad (4.28)$$

$\implies$

$$\frac{\partial A_1}{\partial \tau} = \sigma_1 A_1 + \gamma_1 A_1 \left( [(k_1^4 - l_1^2)|A_1|]^2 + \sum_{j=2}^3 2 \cdot [(k_j^4 - l_j^2)|A_j|]^2 \right) + \alpha_1 A_2^* A_3^*, \quad (4.29)$$

where  $\alpha_1(\vec{k}_1, \vec{k}_2, \vec{k}_3) = \frac{(ck_1^2 + a)(2\lambda(r_3(k_{2x} k_{3x}) + (k_{2y} k_{3y})) + 2\nu(k_2^4 - l_2^2)(k_3^4 - l_3^2))}{ck_1^2 + a - k_1^4 + l_1^2}$

and  $\gamma_1(\vec{k}_1, \vec{k}_2, \vec{k}_3) = \frac{3\eta(k_1^4 - l_1^2)}{ck_1^2 + a - k_1^4 + l_1^2}$

and  $\sigma_1 = \sigma(\vec{k}_1)$ .

Again, equations for  $\frac{\partial A_2}{\partial \tau}$  and  $\frac{\partial A_3}{\partial \tau}$  can be derived from cyclic permutation of the indices.

We are interested in understanding the stable solutions to the above system (i.e.  $\frac{\partial A_i}{\partial \tau} = 0$ ) and at this point several reductions to particular cases can be made. The homogeneous state  $A_1 = A_2 = A_3 = 0$  is the steady state solution  $u = \phi = 0$ . Rolls will be achieved for stable solutions to the amplitude equations where  $A_2 = A_3 = 0$ :

<sup>5</sup>The ODEs for  $A_2$  and  $A_3$  needed to complete the coupled system of amplitude equations can be derived by cyclic permutation of the indices.

$$\frac{\partial A_1}{\partial \tau} = \sigma A_1 + \gamma(k_1^4 - l_1^2)A_1|A_1|^2 = 0 \quad (4.30)$$

which has solutions  $A_1 = \pm \sqrt{\frac{-\sigma}{\gamma(k_1^4 - l_1^2)}}.$

In the isotropic case the complexity of the system of amplitude equations is reduced by applying equivariance under rotation [22]. This forces  $\sigma = \sigma_1 = \sigma_2 = \sigma_3$ ,  $\gamma = \gamma_1 = \gamma_2 = \gamma_3$  and  $\alpha = \alpha_1 = \alpha_2 = \alpha_3$  and enables us to solve explicitly the case where  $A_1 = A_2 = A_3 \neq 0$  corresponding to hexagonal pattern formations [15]. This is more elusive in the anisotropic because the coefficients on the quadratic terms of the amplitude equations are not all equal. In particular the system is not gradient for all parameters and wavevectors. We would like to at least check if, for certain choices of parameters and wavevectors, we can write the amplitude equations as a gradient system. This investigation remains to be carried out.

### 4.3 Persistent Homology Statistics

In this section we will define several standard statistics on barcode data to explore the evolution of a binary surface towards a stable hexagonal array of nanodots.

First consider the idealized scenario; the expected long-term stable solution for some specified set of parameters which give rise to hexagonal ordering. This is a collection of raised dots whose peaks lie precisely on a hexagonal lattice of points in the plane. Since defects in the array come in the form of deviation of the peaks from this lattice, and because of the limitations on the number of points which can feasibly be used as a sample within current PH computational packages we will track only the local maximums of the surface (i.e. the nanodot peaks) as it is altered by ion bombardment.

**Definition 4.3.1.** We can take a planar hexagonal lattice to be a set of points in the plane generated by two vectors (of the same length) such that the angle between them is  $\frac{2\pi}{3}$  radians.

That is

$$\mathbb{H}_{u_1, u_2} = \left\{ m \cdot u_1 + n \cdot u_2 \mid m, n \in \mathbb{Z} \text{ and } \frac{2\pi}{3} = \cos^{-1} \left( \frac{\langle u_1 | u_2 \rangle}{|u_1|^2} \right) \right\}.$$

We observe that within such a lattice, sets of three adjacent points form equilateral triangles with side lengths  $|u_1| = |u_2|$ . Thus for such a set of points we know the structure of the Betti-0 and Betti-1 Rips barcodes.

Consider a square region of the plane containing a planar hexagonal lattice. Assume the subset of the lattice within this region contains  $n$  points. Then we expect for filtration times  $0 \leq t < |u_1|$  there will be  $n$  connected components in the Rips simplicial complexes. At time  $t = |u_1|$  edges of this length are added to the complex and, by the definition of the Rips complex, two dimensional faces (the faces of the equilateral triangles) are also added. In other words, for a true hexagonal lattice without defects, no Betti-1 homology class will appear for any simplicial complex at any filtration time.

However, if we perturb the points of the lattice (i.e. introduce a defect) we can force the appearance of a hole (a topological circle) and thus a bar in the Betti-1 barcode. We illustrate this in Figure 4.3.

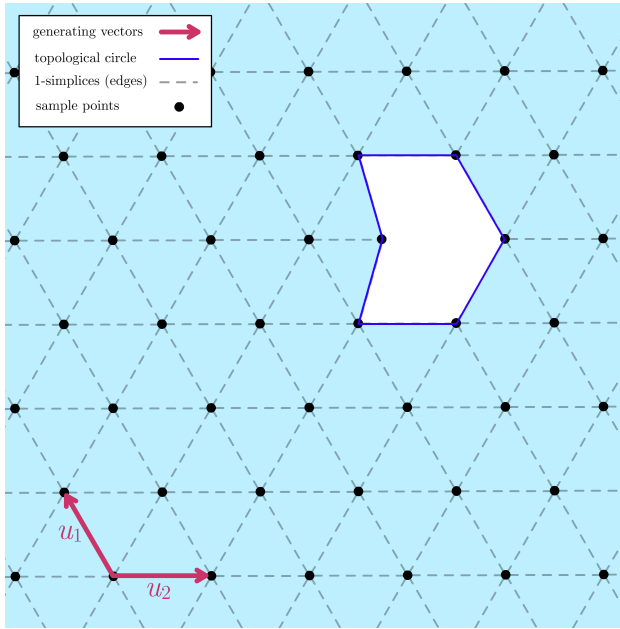


Figure 4.3: A defect in a hexagonal lattice which results in a hole (a topological circle) appearing at filtration time  $t = |u_1|$ .

One observation then is that the more defects, and the greater their severity, the more frequent and the larger the holes in the simplicial complexes may be and thus the longer and more frequent the resulting Betti-1 barcodes. To illustrate this behavior we present Figure 4.4 which shows time series snapshots of a simulated surface as it evolves towards a hexagonal array.

We compare Figure 4.4 to Figure 4.5 which shows a simulated surface undergoing ion bombardment according to the KS equation (with the same domain and parameters) and the associated Betti-0 and Betti-1 barcodes. Notice that in the case of the coupled system of equations the Betti-1 barcodes diminish in total and average length in time and the lengths of the Betti-0 barcodes become more consistent. We formalize these observations by defining some basic barcode statistics and applying them to this system.

**Definition 4.3.2.** Represent the Betti- $j$  barcode data as a set of real intervals,  $\hat{\beta}_j = \{[x_i^j, y_i^j] | 1 \leq i \leq k\}$  where each interval  $[x_i^j, y_i^j]$  represents the bar in the Betti- $j$  barcode which starts at  $x_i^j$  and ends at  $y_i^j$ . Define the **total barcode length** of  $\hat{\beta}_j$  to be  $\text{TotLen}(\hat{\beta}_j) := \sum_{i=1}^k (y_i^j - x_i^j)$ . Further define the **average barcode length** of  $\hat{\beta}_j$  to be  $\text{AvgLen}(\hat{\beta}_j) := \frac{\text{TotLen}(\hat{\beta}_j)}{k}$ .

We can of course define other standard statistics such as the variance in the barcode length and the standard deviation of the barcode lengths in a similar way. In Figure 4.6 we plot the average Betti-1 barcode length from the same simulation as in Figure 4.4 and note its decline towards 0 as the system evolves.

In Figure 4.7 we plot the average Betti-1 barcode length given by a simulation of the Kuramoto-Sivashinsky equation 4.3 over the time interval  $200 \leq t \leq 30,000$  for comparison to the coupled system.

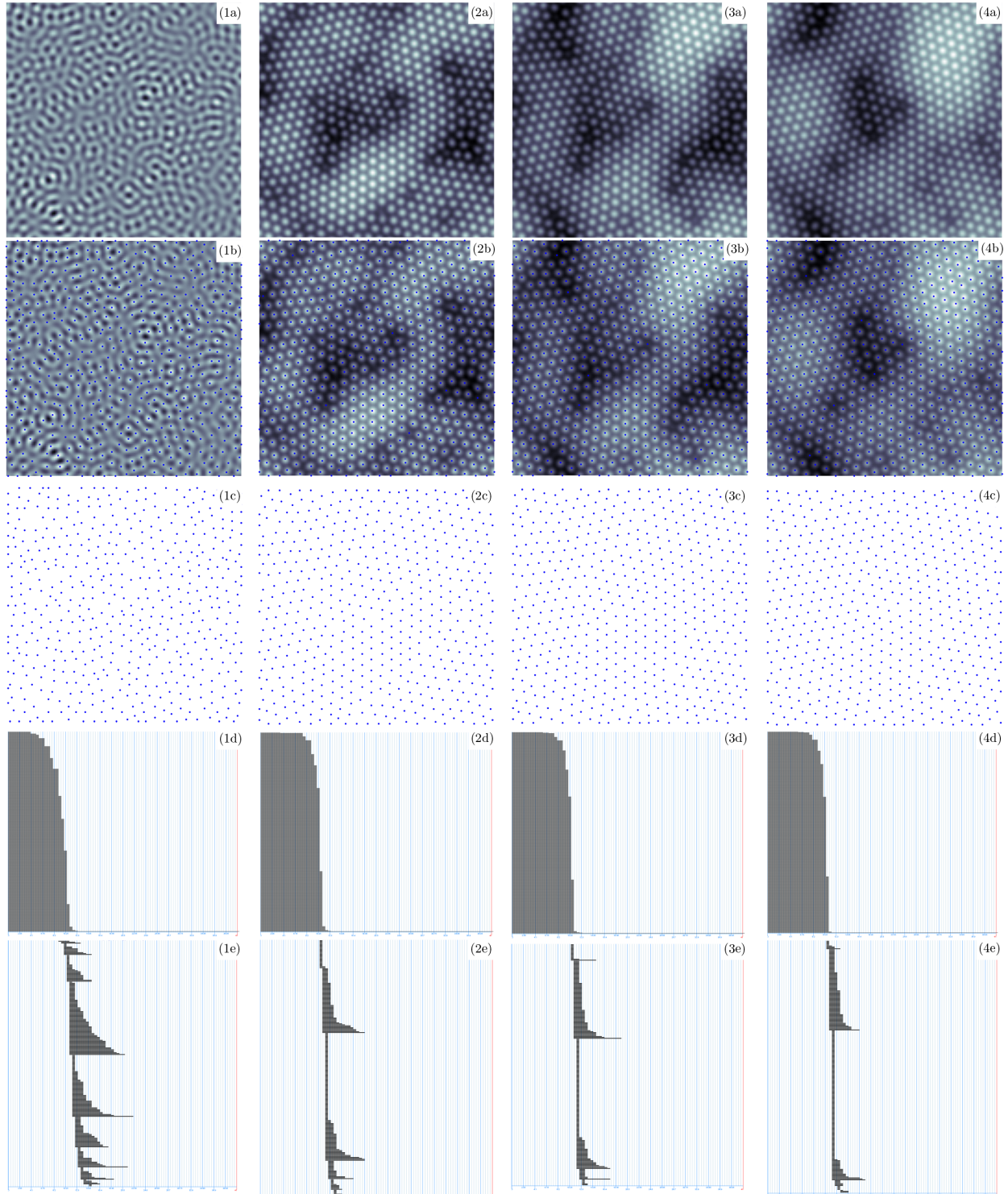


Figure 4.4: A time series of plots of  $u(x, y, t)$  evolving according to the coupled equations 4.1, 4.2 with parameters  $a = .4, c = .6, r_1 = r_2 = r_3 = 1, \lambda = -.3$  in a square region  $(-120 \leq x, y \leq 120)$  at times (1a-e)  $t = 200$ , (2a-e)  $t = 1,800$ , (3a-e)  $t = 9,800$ , (4a-e)  $t = 30,000$ . These show the evolution towards a hexagonal array. (1-4a) shows the surface plots where lighter regions indicate larger values of  $u(x, y, t)$ . (1-4b) shows the same surface plots with the local maxima [17] (peaks of the nanodots) highlighted by a blue dot. (1-4c) shows plots of these peaks with the surface plot removed. (1-4d) are the Betti-0 barcodes generated by the blue points, considered as a sample of the plane. (1-4e) are the Betti-1 barcodes generated by the blue points, considered as a sample of the plane.

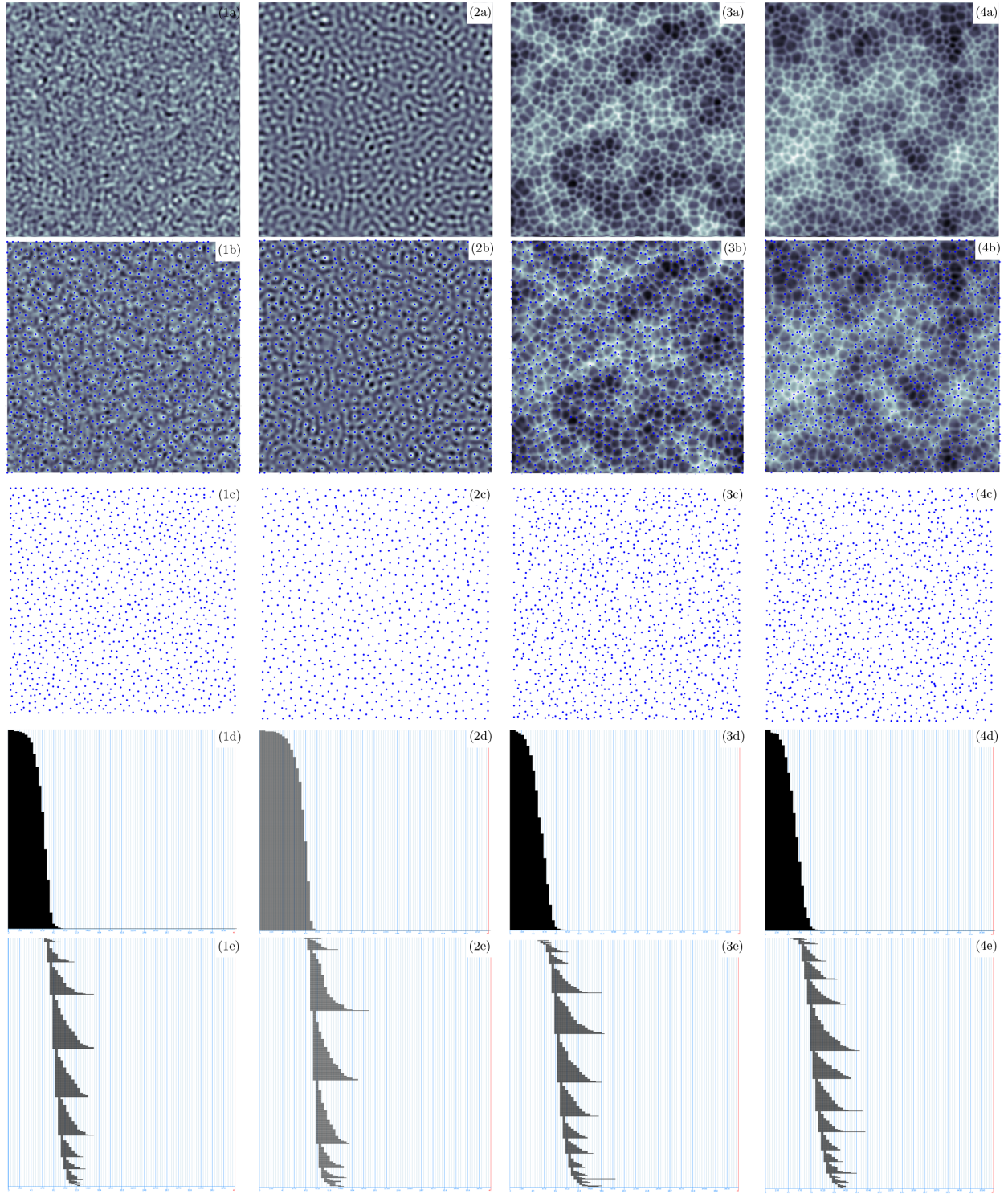


Figure 4.5: A time series of plots of  $u(x, y, t)$  evolving according to the isotropic KS equation 4.3 with parameters  $r_1 = r_3 = 1, \lambda = -.3$  in a square region ( $-120 \leq x, y \leq 120$ ) at times (1a-e)  $t = 200$ , (2a-e)  $t = 1,800$ , (3a-e)  $t = 9,800$ , (4a-e)  $t = 30,000$ . (1-4a) shows the surface plots where lighter regions indicate larger values of  $u(x, y, t)$ . (1-4b) shows the same surface plots with the local maxima [17] (peaks of the nanodots) highlighted by a blue dot. (1-4c) shows plots of these peaks with the surface plot removed. (1-4d) are the Betti-0 barcodes generated by the blue points considered as a sample of the plane. (1-4e) are the Betti-1 barcodes generated by the blue points considered as a sample of the plane.

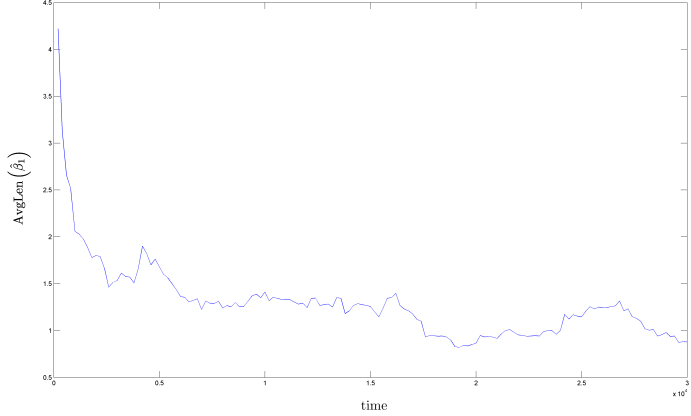


Figure 4.6: Plot of the average Betti-1 barcode lengths as a function of time in timesteps of  $\Delta t = 200$  for the range of times  $200 \leq t \leq 30,000$  for the simulation presented in Figure 4.4

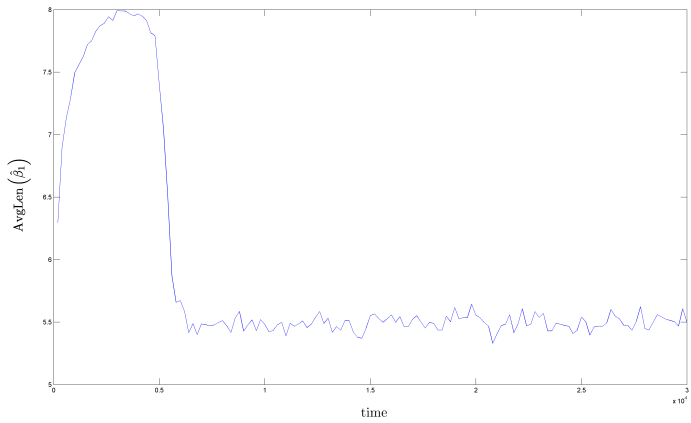


Figure 4.7: Plot of the average Betti-1 barcode lengths as a function of time in timesteps of  $\Delta t = 200$  for the range of times  $200 \leq t \leq 30,000$  for the Kuramoto-Sivashinsky equation with parameters  $r_1 = r_3 = 1, \lambda = -.3$  in the domain  $-120 \leq x, y \leq 120$

## Chapter 5

### IMPROVING PH SAMPLES

As we have stated, one of the principle goals and the original intention of computational homology is to extract coarse topological features of some unknown space from a finite (often noisy) sampling of points from that space. The first step in this process is collecting the sample and so one inherent problem is ensuring that your sample is “good.” For now we will take “good” to mean that the resulting persistence diagrams accurately reflect the topology of the space from which the sample was gathered. For simple spaces, with well defined notions of uniformity, we expect a good sample to be one which is evenly spread across the underlying space so as to maximize the signals that indicate real homology classes and minimize noise or false positives (i.e. persistent barcodes which are the result of unlucky sampling) (see Figure 5.1).

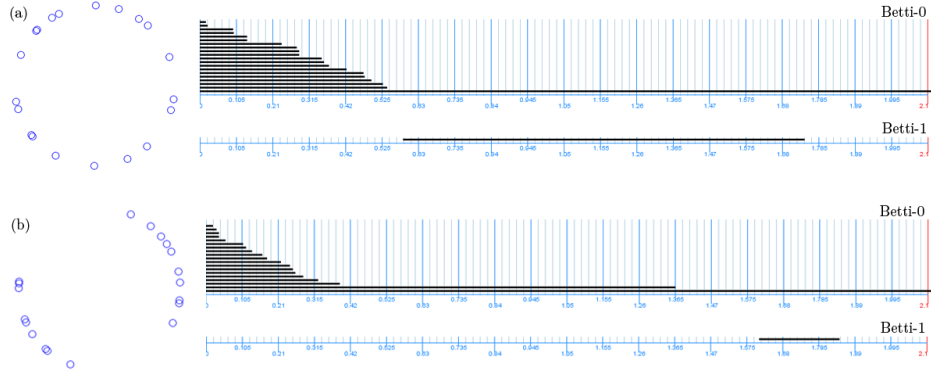


Figure 5.1: Two different samples of circle and their corresponding Betti-0 and Betti-1 barcodes. (a) is an example of an evenly distributed sample while (b) is a poorly distributed sample.

The barcodes in Figure 5.1(b) suggest the underlying space has two connected components and the Betti-1 barcode is much shorter than for the more evenly distributed sample. While this is a toy example it serves to illustrate the point: it is not possible to judge whether

a particular sample is good or bad using only the resulting persistence data (provided that you do not already know the homology of the underlying space). One natural approach, and a source of many interest unanswered questions about this technology, is to simply sample more points. However, the computational complexity of existing algorithms greatly limits the sample size to which PH can be applied. One could try and convince themselves of the accuracy of a result by repeated sampling but this is both time consuming and provides no guarantee of the correctness of the results. Alternatively one could try and improve a sample by some method.

In this section we introduce an approach that aims to rearrange a sample across the underlying space from which it was taken so as to improve the homological signal given by PH. As a proof of concept we develop and implement an algorithm for the particular case where the underlying manifold is the group of orthogonal, real  $2 \times 2$  matrices; a space whose topological structure is known. Before that we construct an elucidating example to introduce and explain the method.

**Example 5.0.1.** Consider the poor sampling of the circle given in Figure 5.1(b). If we imagine these points as being positively charged particles, bound to the underlying space  $S^1$ , and we allow them to move on the circle then their natural tendency will be to spread out into some minimum energy state. We can simulate this behavior by calculating the net force acting on each point charge (according to, for example, Coulomb's law), moving each particle in the direction of this force some small distance, and then normalizing the resulting position to bring the particle back to the unit circle. Figure 5.2 shows the evolution of the poor sample of points under this iterative approach and the corresponding barcodes.

Since any sample of a space to which PH is applied will necessarily come equipped with a distance matrix it is conceivable that sample points can always “push” on each other with some “force” according to a sort of Coulomb's law. The difficulty then, and what will change from problem to problem, is in determining what it means to move points in the direction of this force and in ensuring that points stay on the underlying space.

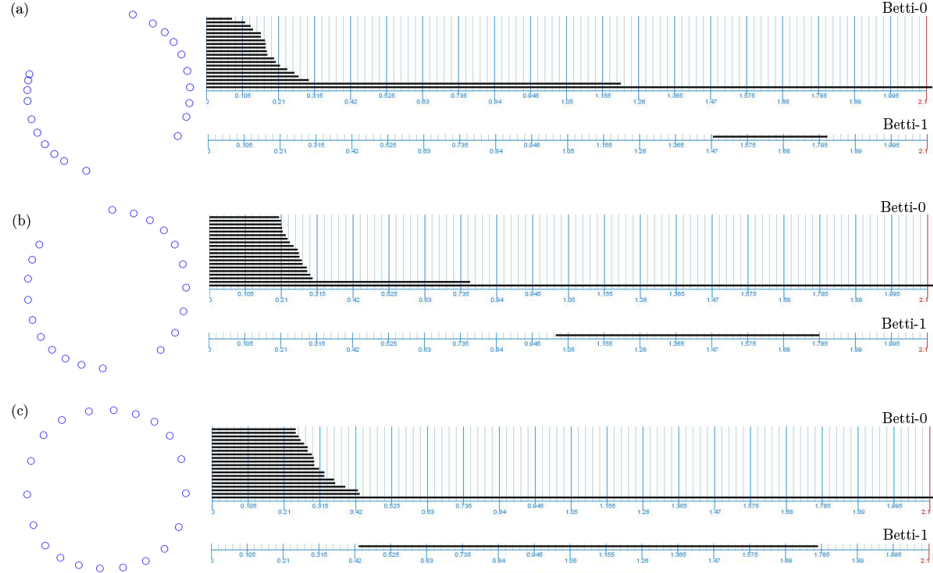


Figure 5.2: Snapshots at iteration numbers (a) 10, (b) 15, and (c) 20, showing the evolution of the position of the sample points as they push against each other according to a  $\frac{1}{r^2}$  Coulomb's law.

We discuss answers to these questions with a space marginally more complicated than  $S^1$ , namely  $O_2(\mathbb{R})$ , and illustrate the impact the process can have on the persistence data.

**Example 5.0.2.** We begin by introducing a standard metric on the space of all matrices. This induces a metric structure on the set  $O_2(\mathbb{R})$  and so provides a method for populating a distance matrix from a random sample of this space.

**Definition 5.0.3.** The **Frobenius norm**  $\|A\|_F = \sqrt{\sum_{i=1}^m \sum_{j=1}^n |a_{i,j}|^2}$  for  $A = [a_{i,j}]_{1 \leq i \leq m, 1 \leq j \leq n}$ , an  $m \times n$  matrix. Define the Frobenius distance between two matrices to be  $\text{dist}_F(A, B) = \|A - B\|_F$ .

Let  $S = \{S_i | 1 \leq i \leq n\} \subset O_2(\mathbb{R})$  be a collection of  $n$  orthogonal matrices. To apply PH to this sample we first construct the distance matrix of all pairwise Frobenius distances between points of  $S$ , that is the matrix  $D = [d_{i,j}]_{1 \leq i, j \leq n}$ , where  $d_{i,j} = \text{dist}_F(S_i, S_j)$ . We can then apply a Rips filtration to construct a family of simplicial complexes whose homological data is displayed as, the now familiar, barcodes.

It is known that  $O_2(\mathbb{R})$  (with topology induced by the Frobenius norm for example) is homeomorphic to two circles [16] (one for each allowable determinant:  $\pm 1$ ). So we expect a “good” sample  $S$  will lead to two persistent Betti-0 bars and two persistent Betti-1 bars. The stronger this signal the better we will say the sample is. Motivated by the circle example we imagine that each matrix has some charge associated to it to define a force field created by the interaction of the  $n$  matrices in our sample.

**Definition 5.0.4.** For each pair  $(S_i, S_j)$  define  $\text{Force}_F(S_i, S_j) = \frac{1}{\text{dist}_F(S_i, S_j)}$ . For each matrix  $S_i \in S$  define  $\text{totForce}_F(S_i) = \sum_{j=1}^n \text{force}_F(S_i, S_j)$ . We note that the naming conventions are chosen to maintain the clarity of the analogy to a physical system while in reality these “forces” are merely positive numbers. Further define  $P(S_i, S_j) = \frac{\text{force}_F(S_i, S_j)}{\text{totForce}_F(S_i)}$ ; that is the fraction of the total force on  $S_i$  exerted by  $S_j$ .

We have in essence defined the magnitudes of the forces of interaction between the matrices in our sample. We now need to define a direction in which these forces act. One approach is to fix two sample points  $S_i, S_j$  and define the matrix  $\hat{S}_i = \alpha S_i + P(S_i, S_j)(1-\alpha)S_j$  to be the new “position” of  $S_i$  after  $S_j$  has “pushed” on  $S_i$ . Notice we have scaled the amount of this displacement by the inverse of the Frobenius distance, maintaining the analogy to Coulomb’s law.

Of course  $\hat{S}_i$  may no longer be an element of  $O_2(\mathbb{R})$  and so we correct back to this space, so as to simulate motion on the manifold itself, by finding the nearest orthogonal matrix to  $\hat{S}_i$  and redefining  $S_i$  to be this matrix. In particular define  $\mathcal{U} : M_{d \times d}(\mathbb{R}) \rightarrow M_{d \times d}(\mathbb{R})$  as  $\mathcal{U}(X) = U \cdot V^*$ , where  $X = U \cdot \Sigma \cdot V^*$  is the singular value decomposition of  $X$ .<sup>1</sup>.

In both examples the effect of this spreading heuristic on the quality of the persistence data is readily apparent. In the example involving orthogonal matrices the two Betti-1 bars

<sup>1</sup> $\mathcal{U}(X)$  is the nearest unitary matrix to  $X$  as measured by any unitarily invariant norm. [18]

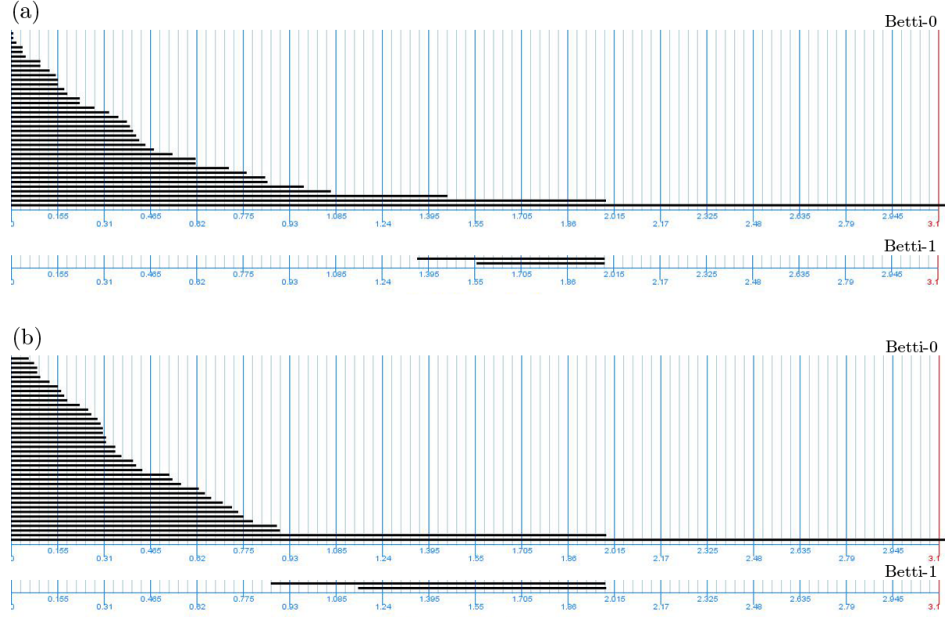


Figure 5.3: (a) Barcodes generated by a random sample of  $n = 40$  orthogonal  $2 \times 2$  matrices and (b) barcodes after the sample is allowed to evolve under iterations of the algorithm described above.

are significantly lengthened and all but two Betti-0 bars are diminished giving a persistence diagram that much better reflects the homology of  $O_2(\mathbb{R})$ .

While the particulars of this methodology will change from problem to problem we highlight the fact that a very similar approach to the first example can be implemented for an entire class of important topological objects: real algebraic varieties.

Given a system of polynomial equations we can consider its set of real solutions as living in some high dimensional real vector space. In this setting the magnitude and direction of the forces of interaction between elements of a sample of solutions are natural generalizations of our simple example on the circle. As we have seen in the above examples this interaction will likely displace our sample off the topological space we are interested in analyzing. However, nonlinear numerical solvers using such approaches as trust-region and conjugate-gradient methods [19] are fast and readily available<sup>2</sup>. Using the displaced point as an initial guess

---

<sup>2</sup>For example in Matlab's optimization toolbox

(which by design would be near the variety) would, in theory, enable us to determine a nearby point on the variety using these numerical optimization techniques, thus allowing us to simulate motion on the object of interest. Through iteration of this process, our goal is to evolve our sample to one which better reflects the topological signals produced by persistent homology.

**Example 5.0.3.** As a second example we demonstrate an implementation of this general technique on a compact surface; the torus given as the zero set of the following equation in three variables,

$$F(x, y, z) = \left(3 - \sqrt{x^2 + y^2}\right)^2 + z^2 - 4 \quad (5.1)$$

We begin with a very poor sampling of 150 points on this torus and then allow each point to be influenced by its nearest neighbors. Again, we think of each point as being a charged particle so that it experiences a repulsive force (governed by Coulomb's law) from the other sample points. New points are found by moving each point a small step in the direction of the net force acting on them and then Matlab's optimization toolbox is used with these new point as initial conditions to calculate nearby points on the torus. In this way motion on the manifold is simulated. Figure 5.4 shows time series snapshots of the sample and the associated barcodes. Here we have plotted barcodes as points in the  $xy$ -plane; the  $x$ -coordinate is the barcode start time and the  $y$ -coordinate is the barcode end time. Thus long barcodes correspond to points far from the  $y = x$  line, while points near the diagonal are weaker signals and can be considered noise.

Although these snapshots do not demonstrate fully the evolution of the barcodes, we note the emergence of two Betti-1 barcodes which move, more or less horizontally, away from the  $y = x$  line before stabilizing. These correspond to the two generators of the Betti-1 homology group which exist for a torus. Initially no simplicial complex in the filtration contains a void but as the points spread noise appears in the Betti-2 barcode and, again, a

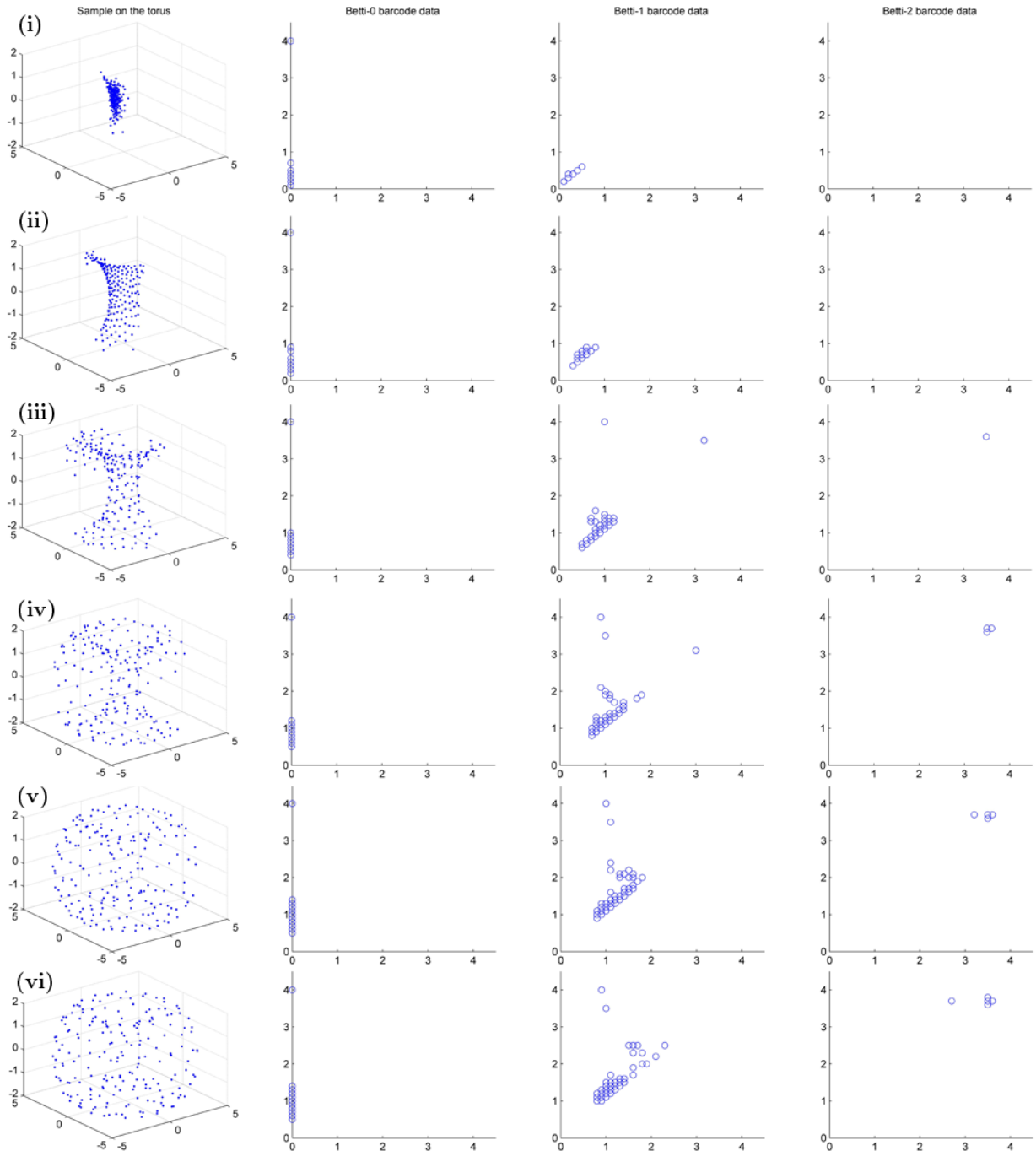


Figure 5.4: Samples of  $n = 150$  points on the torus given by Equation 5.1, Betti-0, Betti-1, and Betti-3 barcodes for the associated sample taken at (i) 1, (ii) 30, (iii) 60, (iv) 90, (v) 120, and (vi) 150 iterations of the spreading procedure.

single point moves horizontally away from the  $y = x$  line as the signal of a single Betti-2 generator (corresponding to the trapped volume in a torus) appears and strengthens.

If we consider a fixed sample size of a fixed metric space it is not known what finite subset (sample) will produce the barcodes that best reflect the topology of the underlying space. The ideal sample may very well differ between barcode dimensions. For simple examples such as the circle and the sphere we expect a distance matrix with minimal variance in the distances between nearest neighbors (i.e. a uniformly distributed sample) will produce the best barcodes. The author sees no reason why this need be the case for every manifold.

Moreover, even for a fixed dimension, the notion of a best barcode is not yet well defined. Nonetheless one would like to be able to answer questions such as: which set of  $n$  points sampled from a sphere gives rise to barcodes which most closely reflects the homology of the sphere? For the torus? A real algebraic variety? And ultimately, can we produce an ideal sample without knowing the underlying topology?

## Chapter 6

### OUTLOOK

In this paper we have introduced several applications of the computational geometry tool, persistent homology, to data sets generated by dynamical systems. The application of PH to the circle map led to the rediscovery of a beautiful and well-known result about the distribution of points in the orbit of this ergodic system. Additionally we have extracted a set of points in the plane from data generated by ion bombardment simulations. By applying PH to this data we have not only suggested new ways of interpreting barcodes by defining barcode statistics, we have also begun to develop a technique to answer questions of interest to physicists about the degree of ordering present in a sample of a binary material after ion bombardment. Finally we have observed some inherent limitations in PH and have started to develop, through simple examples, techniques to improve the technology. Specifically we have implemented algorithms to iteratively spread points on a real algebraic variety and demonstrated that the methodology works to improve the signals in PH barcodes.

Still these ideas are only in their infancy and there are many directions we wish to explore further. In the case of the modified circle map discussed in Section 3 we would like to use PH to truly distinguish between rotation by the golden ratio and  $\sqrt{2}$ , for example. Ultimately we would like to use PH to order the real numbers by some measure of their ergodicity and relate this distinction to the continued fraction expansion of the numbers.

One of the key ideas in constructing the modified circle map is that both temporal and spatial information is tracked. We would like to do the same for other ergodic dynamical systems such as the class of functions called linked twist maps [23]. It has been shown that certain linked twist maps exhibit islands of non-ergodicity in their domain; topological circles in the plane. We hope to explore further what PH can tell us about the behavior of these

systems both by considering them in standard form and by tracking temporal information as well.

The analysis of the amplitude equations is, as of yet, incomplete and requires further attention. We would like to at least be able to check if, for certain choices of parameters and wavevectors we can write the amplitude equations as a gradient system; for a particular choice of parameters does there exist wavevectors which make all the coefficients in the quadratic nonlinearities equal to one another? Also, what is the value of the dispersion relation at these wavevectors? By definition  $\vec{k}_1$  will be an active mode but the same cannot necessarily be said  $\vec{k}_2$ , and  $\vec{k}_3$ . If they are passive modes then what are the absolute values of  $\sigma(\vec{k}_2)$  and  $\sigma(\vec{k}_3)$ ? Answering this question might give us insight into how hexagonal ordering can be achieved in the anisotropic case.

There are several questions of interest to the applied physics community which might have answers in PH techniques. Dr. Mark Bradley has suggested applying this tool to identify penta and hepta defects in disordered hexagonal lattices, to the problem of classifying viral structures and large molecules, and to fingerprint data. In the same vein Dr. Patrick Shipman has suggested applying PH to objective structures. Also, in this paper, we have only compared models of ion bombardment. We would like to utilize PH to further compare these models with the numerous examples of real-world experiments which demonstrate spontaneous pattern formation for both normal and off-normal-incidence ion bombardment of a solid surface. This has the potential to lead to a quantitative measurement of the degree of ordering in nanostructures.

Towards the goal of improving a sample of point-cloud data from a topological manifold, Dr. Shipman has speculated that one may be able to evolve the Swift-Hohenberg equation or another appropriately chosen PDE to a stable solution which gives a good sampling. The problems of minimal surfaces, packings, and (more generally) of the calculus of variations may find a place to grow in computational topology.

The major commonality between these objectives is that they all attempt to build connections between dynamical systems and computational topology. A natural, albeit very broad, overarching question common to the ideas contained in this paper is how do barcodes evolve as the input sample changes? This question is of particular interest and is one which we hope to explore in the future.

## Bibliography

- [1] J. Matousek. Using the Borsuk-Ulam theorem: lectures on topological methods in combinatorics and geometry. Springer-Verlag Berlin Heidelberg. p 16.
- [2] G. Carlsson, Topology and data. American Mathematical Society 46.2 (2009): 255-308.
- [3] A. Hatcher. Algebraic Topology. Cambridge University Press, 2002.
- [4] J. Leray. Sur la forme des espaces topologiques et sur les points fixes des reprsentations. J. Math. Pures Appl. 24:95167, 1945.
- [5] R. Bhatia. Fourier Series. The Mathematical Association of America, 2005.
- [6] P. D. Shipman, Discrete and continuous invariance in phyllotactic tilings. Physical Review E. **81**, 031905 (2010).
- [7] G.H. Hardy, E.M. Wright. An Introduction to the Theory of Numbers. Oxford University Press, 2008.
- [8] graphicalanalysis.m package, by Thomas LoFaro, tlofaro@gustavus.edu. Copyright 2001, Thomas LoFaro.
- [9] E. Chason, W. L. Chan, Spontaneous patterning of surfaces by low-energy ion beams, Topics Appl. Physics 116 (2010) 53-71.
- [10] B. Ziberi, M. Cornejo, F. Frost, B. Rauschenbach, Highly ordered nanopatterns on Ge and Si surfaces by ion beam sputtering, J. Phys. Condens. Matter 21 (2009) 224003.
- [11] S. Facsko, T. Dekorsy, C. Koerdt, C. Trappe, H. Kurz, A. Vogt, H. L. Hartnagel, Formation of ordered nanoscale semiconductor dots by ion sputtering, Science 285 (1999) 1551-1553.

- [12] F. Frost, A. Schindler, F. Bigl, Roughness evolution of ion sputtered rotating InP surfaces: Pattern formation and scaling laws, Phys. Rev. Lett. 85 (2000) 4116-4119.
- [13] M. Castro et al., Phys. Rev. Lett. 94, 016102 (2005).
- [14] S. Facsko et al., Phys. Rev. B 69, 153412 (2004).
- [15] R. M. Bradley, P. D. Shipman, Spontaneous Pattern Formation Induced by Ion Bombardment of Binary Compounds. Phys. Rev. Lett. 105, 145501 (2010).
- [16] V.A. Zorich, Mathematical analysis, Volume 2. Springer-Verlag Berlin Heidelberg, 2004. p. 324.
- [17] extrema.m, extrem2.m packages, by Carlos Adrin Vargas Aguilera, nubeobscura@hotmail.com. Physical Oceanography MS candidate, Universidad de Guadalajara Mexico, 2004.
- [18] K. Fan and A. J. Hoffman, Some metric inequalities in the space of matrices. Proceedings of the American Mathematical Society **Vol. 6 No. 1**, (Feb. 1955) pp. 111-116.
- [19] T.F. Coleman, Y. Li, An Interior, Trust Region Approach for Nonlinear Minimization Subject to Bounds. SIAM Journal on Optimization, **Vol. 6**, (1996) pp. 418-445.
- [20] F.C. Motta, P.D. Shipman, R.M. Bradley, Highly Ordered Nanoscale Surface Ripples Produced by Ion Bombardment of Binary Compounds. to be published, 2012: J. Phys. D: Appl. Phys.
- [21] Strogatz, Steven. Nonlinear Dynamics and Chaos. Westview Pr, (2000) pp. 343-353 160.
- [22] Hoyle, Rebecca B. Pattern formation: an introduction to methods. Cambridge University Press, (2006) pp. 134-167.
- [23] J.M. Ottino, R. Sturman, S. Wiggins. The Mathematical Foundations of Mixing: The Linked Twist Map as a Paradigm in Applications: Micro to Macro, Fluids to Solids. Cambridge University Press, 2006.